



Chemical Fractionation Modeling of Plumes Indicates a Gas-rich, Moderately Alkaline Enceladus Ocean

Lucas M. Fifer¹, David C. Catling¹, and Jonathan D. Toner¹Department of Earth and Space Sciences, University of Washington, Seattle, WA 98195, USA; lufifer@uw.edu

Received 2021 July 18; revised 2022 June 12; accepted 2022 June 17; published 2022 August 11

Abstract

Enceladus harbors an ocean beneath its ice crust that erupts spectacular plumes from fissures at the south pole. The plume composition was measured by the Cassini spacecraft, and provides evidence for the ocean's gas content, salinity, pH, and potential for life. Understanding the ocean's composition is complicated by physicochemical processes that alter the plume composition during eruption, such as water vapor condensation in the icy fissures and gas exsolution from the ocean surface. We developed a model that includes key fractionation processes, in particular fractionation during gas exsolution, which has not been previously considered. Our model predicts a moderately alkaline (pH 7.95–9.05), gas-rich ocean ($\sim 10^{-5}$ – 10^{-3} molal) with high concentrations of ammonium ions (10^{-2} – 10^{-1} molal). Our derived dissolved gas concentrations are higher than in recent studies because we account for gas exsolution, which depletes gases in the plume compared to the ocean, and because our model conserves mass flow rates between gas exsolution from the ocean and eruption from the tiger stripe fissures. We find carbon dioxide and hydrogen concentrations that could provide sufficient chemical energy for oceanic life in the form of hydrogenotrophic methanogens. Carbon dioxide concentrations of 10^{-5} – 10^{-3} molal indicate a more Earth-like pH than the pH ~ 8.5 – 13.5 in previous studies. The inferred bulk ammonium and total inorganic carbon concentrations are consistent with cometary levels. This corroborates evidence from cometary deuterium-hydrogen (D/H) ratios that Enceladus formed from comet-like planetesimals. Our results suggest a gas-rich ocean that inherited its high volatile concentrations from comet-like building blocks.

Unified Astronomy Thesaurus concepts: [Astrobiology \(74\)](#); [Saturnian satellites \(1427\)](#); [Chemical abundances \(224\)](#); [Water vapour \(1791\)](#); [Comet volatiles \(2162\)](#); [Methane \(1042\)](#); [Carbon dioxide \(196\)](#)

1. Introduction

1.1. Background

Enceladus' plumes are actively erupting in the south polar region from ~ 100 km long 'tiger stripe' fissures (Porco et al. 2006). The plume vapor composition has been measured during several flybys by Cassini's Ion and Neutral Mass Spectrometer (INMS; Waite et al. 2006, 2009, 2017), and solid particles have been analyzed by the Cosmic Dust Analyzer (CDA; Postberg et al. 2009, 2011, 2018; Khawaja et al. 2019). The presence of sodium and potassium salts in the plume indicates an oceanic source with a salinity and approximate composition of 0.05–0.2 molal NaCl, and 0.01–0.1 molal Na_2CO_3 or NaHCO_3 (Postberg et al. 2009). Studies of the moon's orbital libration indicate that this ocean is likely global, decoupling the rocky core from the ice shell (Thomas et al. 2016). Tidal forces provide heat to maintain this ocean over long timescales (Choblet et al. 2017), and lead to the formation of tiger stripe stress fractures through which plume material erupts (Hemingway et al. 2019). Modeling suggests that the ocean partially fills the fissures and is the source of the plumes (Kite & Rubin 2016; Nakajima & Ingersoll 2016).

The plumes of Enceladus inform our understanding of the chemical conditions in the subsurface ocean, but fractionation processes create compositional differences between the plume and ocean (Glein et al. 2015; Bouquet et al. 2019; Glein & Waite 2020). In this paper, we focus on two fractionation

processes that alter the composition of the plume gas during its journey: condensation of water vapor on fissure sidewalls and different rates that gases exsolve from the ocean (which has not been as extensively modeled in previous studies). We build numerical models of plume eruption that incorporate these fractionation effects to predict possible ocean compositions from the plume composition measured by the Cassini spacecraft.

1.2. Plume Composition Measured by Cassini

The gas component of the plume is primarily water vapor (H_2O), with smaller amounts of hydrogen (H_2), carbon dioxide (CO_2), methane (CH_4), and ammonia (NH_3) (see Table 1). The H_2 and CO_2 detected by the INMS are a potential source of chemical energy. In principle, life could use chemical energy in the H_2 - CO_2 redox pair for methanogenesis (McKay et al. 2008; Waite et al. 2017; Affholder et al. 2021; Higgins et al. 2021). CDA analysis of the plume ice grains and INMS analysis of the plume gas found high-mass hydrocarbons (Postberg et al. 2018), and lower-mass oxygen- and nitrogen-bearing organics (Magee & Waite 2017; Bouquet et al. 2019; Khawaja et al. 2019). These organics could be a product of life, or could fuel life in the ocean.

The composition and concentration of dissolved gases in the ocean reveal Enceladus' internal physical processes and potential for biology. The concentration of CO_2 in the ocean is crucial for understanding the ocean's chemistry and habitability (Glein & Waite 2020). CO_2 lowers pH by reacting with water to form carbonic acid (H_2CO_3). Ocean pH impacts not only the viability of life on Enceladus (near-neutral pH often correlates with diversity of terrestrial microbial

Table 1
Measured Gas Abundances in Enceladus' Plume

Species	Volume Mixing Ratio (%)
H ₂ O	96–99
CO ₂	0.3–0.8
CH ₄	0.1–0.3
NH ₃	0.4–1.3
H ₂	0.4–1.4

Note. From Waite et al. (2017).

communities; Keller & Zengler 2004; Fierer & Jackson 2006), but also the speciation of other dissolved ions. In particular, the aqueous speciation of ammonia is a function of pH. In the presence of free protons (H⁺), NH₃ will protonate to form ammonium (NH₄⁺), and both NH₃ and NH₄⁺ are key in terrestrial metabolism (Hoch et al. 1992). Because the negative log of the equilibrium constant (pK_a) for the NH₃ + H⁺ ⇌ NH₄⁺ reaction is ~10.1 (at 273 K; Bates & Pinching 1949), having an ocean pH above or below this value will determine whether NH₃ (>10.1) or NH₄⁺ (<10.1) dominates, and therefore the availability of these species for biology. Modeling of ocean chemistry and analysis of the erupted plume composition has produced a range of pH estimates (see Section 1.3), from acidic to highly alkaline (Marion et al. 2012; Glein et al. 2015), so that the implied NH₄⁺ concentrations have varied widely. The wide range in ocean chemistry estimates from previous studies reflects the disparate ways plume fractionation has or has not been accounted for, which we will explore in Section 1.3.

Other gases in the plume are evidence of hydrothermal, and possibly biological, processes occurring in the ocean. Together, CH₄ and H₂ suggest hydrothermal activity at the base of Enceladus' ocean (Waite et al. 2017). Three possible sources could account for methane. Hydrogenotrophic methanogens consume CO₂ and H₂ and could produce the CH₄ (McKay et al. 2008; Taubner et al. 2018; Affholder et al. 2021). Methanogens on Earth thrive in anoxic environments, and their metabolic pathway is one of the earliest known metabolisms on Earth (Baptiste et al. 2005). Alternatively, methane may be produced abiotically via Fischer–Tropsch-type reactions (McCullom & Seewald 2006) associated with hydrothermal environments, although more recent studies find that abiotic production of methane in hydrothermal environments may be limited in the absence of a hydrogen vapor phase (McCullom 2016; see also Bradley 2016; Reeves & Fiebig 2020). Finally, the methane could be primordial like in comets (McKinnon et al. 2018). Better constraints on the concentrations of these gases in the ocean can help to reveal their and Enceladus' origins, by comparison with typical volatile budgets of planet-forming materials.

1.3. Fractionation in the Gas Phase of the Plume

While measurements of specific chemical species in the plume allow us to infer their presence in the ocean, the concentrations of chemical species can differ between the ocean and plume due to fractionation. Fractionation causes certain plume components to erupt preferentially while leaving others behind, resulting in

differing ocean and plume compositions. Therefore direct extrapolation of concentrations in the plume to those in the ocean could be inaccurate. Understanding fractionation is important for future missions that propose to sample Enceladus' plumes because it would allow us to translate improved measurements of the plume (Reh et al. 2016; Cable et al. 2021; MacKenzie et al. 2021) into a more complete picture of the ocean's characteristics. Here, we focus on two fractionation effects: water vapor condensation and differential gas exsolution.

Water vapor will condense out of the plume and onto the walls of the fissure as it travels upwards, enriching the relative concentrations of other gases (CO₂, CH₄, NH₃, and H₂) that do not condense significantly (Glein et al. 2015). In general, at equilibrium, the pressure and density of water vapor in contact with liquid water or solid ice is set by the temperature of the liquid or solid phase (Murphy & Koop 2005). If the pressure in the gas phase is less than this equilibrium value (the “saturation vapor pressure”), then evaporation or sublimation into the gas phase will occur; if the pressure in the gas phase is greater than the saturation vapor pressure, then condensation will occur. In Enceladus' plume, water vapor condensation is expected to occur because of the temperature difference between the base of the fissure (where ice meets the ocean) and the plume outlet at Enceladus' surface (Glein et al. 2015; Nakajima & Ingersoll 2016). As the plume vapor moves upwards through a fissure that is colder toward the surface, the plume vapor will become supersaturated with respect to the ice, and water will condense out of the plume onto the walls to restore equilibrium. The temperature of the ocean can be estimated from the freezing point of a moderately saline ocean, around 273 K, with salinity estimates of the ocean coming from the measured salt concentrations in the plume ice grains (Postberg et al. 2009). The temperature at the plume outlet is 197 ± 20 K based on infrared observations taken by Cassini of the tiger stripes (Goguen et al. 2013).

Glein et al. (2015) use the temperature difference between the ocean and plume outlet to estimate the vapor condensation that occurs during eruption. They assume instantaneous equilibration, so that the density of water vapor at any vertical height within the plume is equal to the saturation vapor density of the ice walls. Using this model, Glein et al. (2015) estimate that the plume loses >99% of its water vapor due to condensation.

Because condensation tends to remove water vapor without significantly affecting the other gases, condensation should produce an erupted plume with enriched concentrations of nonwater gases, which could cause overestimates of oceanic gas concentrations if not accounted for. Marion et al. (2012) do not account for vapor condensation. Instead, they assume that the plume gases are in equilibrium with the ocean. As a result, they predict relatively high gas concentrations in the ocean, including dissolved CO₂, and consequently an acidic ocean pH of 5.74–6.76.

By contrast, studies that accounted for water vapor condensation suggest that nonwater gases dissolved in the ocean are more dilute than in the plume. For example, Glein et al. (2015) predict a highly alkaline pH, 10.8–13.5. Other estimates for ocean pH include 8.5–9, from the distribution of salts in the plume ice grains (Postberg et al. 2009), and 8.5–10.5, from conditions necessary to form silica nanoparticles that were measured streaming away from the Saturnian

system (Kempf et al. 2005), and thought to originate from Enceladus (Hsu et al. 2015). Glein & Waite (2020) find that an ocean pH range of 8.5–9 provides the best fit to both the CDA analysis of salts in the plume ice grains (Postberg et al. 2009) and activity estimates for oceanic CO₂ from INMS data (after accounting for water vapor condensation out of the plume).

Gas exsolution has not yet been adequately explored but will cause further fractionation between plume and ocean concentrations. The production of plume water vapor and all plume gases are driven by differences in partial pressures between their aqueous forms in the ocean and the plume gas above it. Furthermore, differential rates of gas exsolution will fractionate gases between the aqueous and gas phases. Consequently, rapidly exsolving gases are likely enriched in the plume and slowly exsolving gases are depleted in the plume. Rates of gas exsolution can be measured experimentally or calculated via a theoretical model such as a thin-film model, wherein the rate of mass transfer is set by the rate of diffusion (theoretically or experimentally determined) over a hypothetical thin film (with experimentally determined thickness) that lies at the interface of the liquid–gas phase boundary (Cussler 2009). Because it is far more abundant than other volatiles, water enters the gas phase of the plumes at a much greater rate than other gases exsolve. Consequently, water should be enriched in the plume, and any extrapolation of plume measurements that does not account for this would underestimate dissolved gas concentrations. Gas exsolution in the Enceladus ocean–plume system counteracts the loss of water via condensation; condensation of water vapor tends to deplete the plume in water vapor relative to other gases, while gas exsolution tends to enrich the plume in water vapor.

In the rest of the paper, we outline our modeling methods used to quantify fractionation that occurs during (1) condensation of water vapor as the plume erupts through the ice fissures (Sections 2.1, 2.2), and (2) dynamic gas exsolution at the ocean–plume boundary (Section 2.3). We model these fractionation steps in the reverse order of occurrence during eruption because our goal is to begin with the measured plume composition as model input and produce an ocean composition as model output. In this modeling scheme, outputs of the condensation model are used as inputs to the gas exsolution model. We also outline how we model aqueous speciation in Enceladus’ ocean (Section 2.4). Then we describe the results of our modeling efforts, and compare our predictions for ocean composition to previous studies (Section 3). Finally, we consider the implications of our results for Enceladus’ origin and its chemical energy for life (Section 4).

2. Methods

2.1. Water Vapor Condensation Model

To quantify water vapor condensation, we adopt the model of Nakajima & Ingersoll (2016) for plume formation, eruption, and partial condensation. This model assumes that liquid water partially fills the tiger stripe fissures and evaporates, and the resulting plume gas accelerates toward Enceladus’ surface due to strong pressure gradients (Figure 1(a)). In the past, some studies have proposed that a solid source could generate the plumes via ice sublimation and/or clathrate decomposition (Kieffer et al. 2006; Nimmo et al. 2007). However, the detection of salt-rich ice grains (Postberg et al. 2009) and silica nanoparticles in the plume (Hsu et al. 2015) strongly indicate

that a liquid ocean in direct contact with a rocky core is the source of the plume (see also Spencer et al. 2018, for a review of the present state of knowledge of the plume source). In modeling the gas phase dynamics, we approximate the gas as pure water vapor, as in Nakajima & Ingersoll (2016), due to the low mixing ratios of nonwater gases (Table 1). During transport to the surface, plume water vapor condenses on the conduit walls. We assume that solid ice grains in the plume are formed via rapid freezing of aerosol-like ocean droplets that are flung from the ocean surface due to bubbling, boiling, or turbulence (Postberg et al. 2009). These particles get carried by the plume gas.

To estimate the importance of condensation onto ice grains in the plume versus the walls of the fissure, we find a ratio in the total surface areas of these two condensation sites. We calculate this ratio by approximating the grains as spherical particles 1 μm in size (Postberg et al. 2009) and with density equal to that of pure ice, approximated as the density at the freezing point, $\rho_{\text{ice}} \approx 917 \text{ kg m}^{-3}$. The assumption of an approximately pure ice composition is justified given that even the most salt-rich ice grains are >98% water-ice (Postberg et al. 2009). With the above particle radius and density, we can estimate an average grain surface area $SA_{\text{grain}} = 1.26 \times 10^{-11} \text{ m}^2$, average grain volume $V_{\text{grain}} = 4.19 \times 10^{-12} \text{ m}^3$, and average grain mass $m_{\text{grain}} = 3.84 \times 10^{-9} \text{ kg}$. We then use the observed dust-to-gas mass ratio, $R_{\text{dust-to-gas}} \approx 10\%$ (Hedman et al. 2018), and the plume vapor density ρ_{gas} (an output of the model described in the following paragraphs) to find the number density of grains in the plume within the plume conduit at a given moment, $n_{\text{grains}} = R_{\text{dust-to-gas}}\rho_{\text{gas}}/m_{\text{grain}}$. The total surface area of all ice grains in the conduit at a given moment can be expressed as

$$SA_{\text{tot. grains}} = SA_{\text{grain}}n_{\text{grains}}DL\delta, \quad (1)$$

where D is the total distance from the ocean–plume boundary to the plume outlet, L is the length of the fissure, and δ is the (thin) width of the fissure (Figure 1(b)). The surface area of the fissure walls can be expressed as

$$SA_{\text{walls}} \approx 2DL, \quad (2)$$

neglecting the small end wall area ($2D\delta$). The ratio of ice grain surface area to fissure walls is thus

$$f = \frac{SA_{\text{tot. grains}}}{SA_{\text{walls}}} = \frac{SA_{\text{grain}}n_{\text{grains}}\delta}{2}. \quad (3)$$

Using Equation (3), we find that the ratio of ice grain surface area to wall surface area that the plume vapor encounters during eruption is about 1:10⁹. This is a conservative estimate as it assumes that the ice grains are stationary (and that the plume vapor “sees” all grains in the conduit), but in reality the ice grains are moving upward as well, being carried in the plume gas such that the plume vapor will only “see” a fraction of all ice grains in the conduit. From the ratio of surface areas that we calculate, we posit that vapor condensation onto the solid ice grains is negligible compared to condensation onto the walls of the conduit.

The model of plume eruption (Nakajima & Ingersoll 2016) includes conservation of mass, momentum and energy, expressed through Equations (A1)–(A3) listed in Appendix A. These three equations, along with an equation for the internal energy ($du = C_v dT$, where u is the internal energy, C_v is the specific heat capacity of water vapor at constant volume, and T is

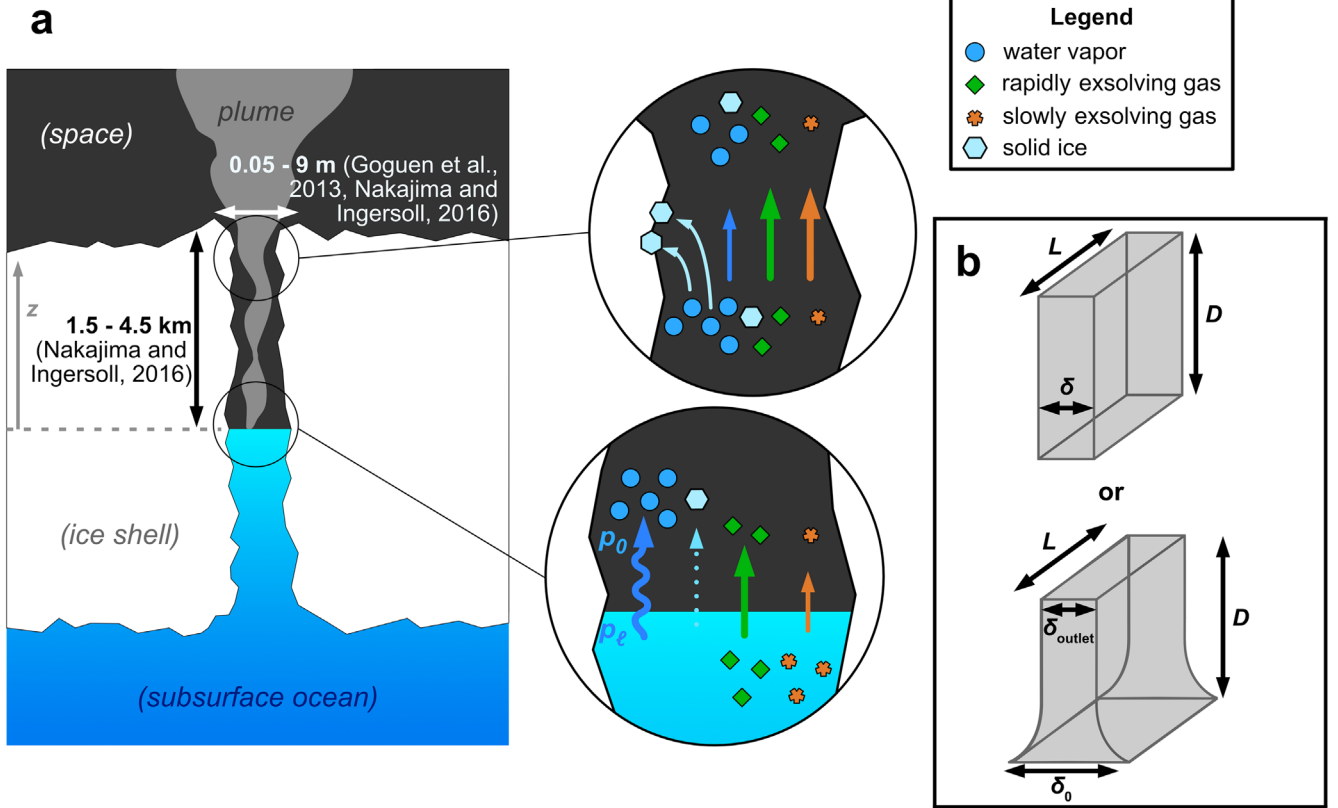


Figure 1. (a) A diagram showing the ocean source to Enceladus’ plumes, and two key fractionation processes. In the lower-right circle, water evaporation and gas exsolution occur at different rates, enriching the plume in water vapor and those gases that exsolve rapidly. The vapor pressure of the liquid (p_ℓ) is larger than the partial pressure of water vapor directly above the ocean (p_0), driving evaporation (Nakajima & Ingersoll 2016). Solid ice grains in the plume are formed via freezing of aerosol-like droplets of water, and carried in the plume gas (Postberg et al. 2009). In the upper-right circle, water vapor condenses out of the plumes onto the walls of the ice fissures, whereas other gases do not condense out significantly (Glein et al. 2015). (b) Diagrams of the modeled fissure geometries, with depth D measured from the surface to the ocean—plume boundary, fissure length L , and either constant diameter δ or a tapering diameter starting from δ_0 at the ocean and narrowing to δ_{outlet} at the plume outlet (see Equation (6)).

the temperature of the plume), ideal gas law, and temperature-dependent saturation vapor pressure p of ice at absolute temperature T ,

$$p = 3.63 \times 10^{12} \text{ Pa} \times \exp(-6137 \text{ K}/T), \quad (4)$$

are used to find expressions for the terms dT/dz , du/dz , ds/dz , $d\rho/dz$, dp/dz , and dv/dz . Here z is the vertical distance from the gas–water interface at the bottom of the fissure (Figure 1), s is the solid mass fraction of the plume, ρ is the density, p is the pressure, and v is the velocity. Equation (4) assumes that the vapor is approximately at pressure equilibrium with the ice walls throughout the conduit, which is justified given that the expected equilibration times are on the order of milliseconds (Ingersoll & Pankine 2010). With these expressions, we use a finite-difference method beginning from the ocean–plume boundary, calculating each $d(X)/dz$ term iteratively (where $(X) = T, u, s$, etc.), stepping upward through the fissure by small (typically ~ 1 meter) distances Δz .

For the lower boundary, at the ocean–plume interface, we use the following equation

$$\rho_0 v_0 \delta_0 = \frac{(p_\ell(T_\ell) - p_0)}{\sqrt{2\pi RT_\ell/M}} \delta_0, \quad (5)$$

from Nakajima & Ingersoll (2016) to determine the rate of water evaporation. In Equation (5), the subscript ℓ represents a

parameter of the liquid water, and the subscript 0 represents a parameter of the bottommost numerical “cell” of the plume vapor. Here δ is the diameter of the fissure, R is the universal gas constant, and M is the molar mass of water. Equation (5) is a form of the Hertz relation (Persad & Ward 2016), wherein a Maxwell–Boltzmann distribution is assumed for particle velocities in both the liquid and gas phase, and mass transfer between phases is determined by the frequency with which particles collide with the phase boundary.

As in Nakajima & Ingersoll’s (2016) work, we initialize the model by guessing a value for the plume gas pressure directly above the ocean (p_0). We use the bisection method to iteratively guess p_0 , until we find a solution for all variables (T, u, s, ρ, p, v) as a function of z such that the plume velocity v at the outlet is within the range of the escape velocity from Enceladus’ surface and the sound speed (given by $v_{\text{sound}} = \sqrt{\gamma RT/M}$, where γ is the ratio of specific heat capacity at constant pressure to specific heat capacity at constant volume, taken to be 1.333 for water vapor). The escape velocity is taken as a lower limit because the erupting plume vapor is observed to escape from Enceladus, while some fraction of the slower ice grains fall back to the surface (Kempf et al. 2010; Hansen et al. 2020). The speed of sound is taken as an upper limit to the plume velocity because one-dimensional flow of gas through a long pipe should remain below the speed of sound as long as the initial velocity (in this case, of the plume evaporating at the

ocean surface) is below the speed of sound (Landau & Lifshitz 1959; Nakajima & Ingersoll 2016). For additional details of the condensation model, see Appendix A, and our code, which we have made open source.

Observed heat fluxes from the south polar terrain and mass fluxes of the eruptions provide constraints on other model parameters, such as the geometry of the tiger stripe fissures. The temperature of the fissure walls, which decreases toward the outlet, is found using Equations (A4)–(A8). In these equations, the heat generated by condensation is assumed to be responsible for the elevated heat fluxes observed in Enceladus' south polar terrain in the vicinity of the tiger stripe fissures (Nakajima & Ingersoll 2016). We consider a range of possible fissure geometries, with fissure depths (D) ranging from 1000 meters to 5000 meters, and fissure outlet diameters (δ_{outlet}) ranging from 0.05–0.1 m because these ranges allow the model to match the measured material fluxes (Hansen et al. 2017, 2020; Teolis et al. 2017). Across the different model trials we also vary the diameter of the fissure at the ocean–plume interface (δ_0) from 0.05–1000 m, and the tapering rate of the fissure diameter ($d\delta/dz$). Following the work of Nakajima & Ingersoll (2016), we include models with both an unchanging fissure diameter ($d\delta/dz = 0$ so that $\delta(z) = \delta_0 = \delta_{\text{outlet}}$), and an exponentially narrowing fissure where the tapering rate is defined by

$$\frac{d\delta}{dz} = \delta_{\text{outlet}} + (\delta_0 - \delta_{\text{outlet}}) \exp\left(-\frac{z}{Y}\right). \quad (6)$$

Here, Y is a constant in units of meters (varied from 1–100 m) that corresponds roughly to the vertical distance over which the fissure narrows to its outlet diameter.

2.2. Effect of Vapor Condensation on Plume Gas Composition

The model of plume vapor production and partial loss via condensation provides us with five key outputs that we then use to calculate the initial *plume gas* composition, in the early stages of eruption just above the liquid water interface. The key outputs of the condensation model are the partial pressure of water (p) at both the ocean–plume boundary and at the plume outlet, the evaporation rate at the ocean–plume boundary ($\Phi_{\text{H}_2\text{O, evaporation}}$), the eruption rate ($\Phi_{\text{H}_2\text{O, eruption}}$) of water vapor at the plume outlet, as well as the pressure difference across the ocean–plume boundary ($\Delta p = p_\ell - p_0$, where p_ℓ is the vapor pressure of the liquid ocean). The eruption rate predicted by the model is also used to constrain which fissure geometries are most likely, as in Nakajima & Ingersoll (2016). With these key parameters in hand, we use the following equations to determine how relative abundances of plume gases are altered by condensation.

We note that under the assumption of negligible condensation for all nonwater gas species i , the exsolution rates (in units of kilograms per second in our calculations) for these gases from the ocean should be equal to the eruption rates seen from the fissure outlet, establishing mass conservation for the nonwater gases

$$\Phi_{i, \text{exsolution}} = \Phi_{i, \text{eruption}}. \quad (7)$$

Here, $\Phi_{i, \text{exsolution}}$ is the exsolution rate of nonwater gas species i from the exposed area of the ocean filling the tiger stripe fissure, and $\Phi_{i, \text{eruption}}$ is the eruption rate from the plume outlet at the surface of Enceladus.

With the goal of finding the molar mixing ratios of gases just above the ocean–plume boundary, we can reframe Equation (7) in terms of ocean-to-plume evaporation and plume-measured eruption rates of water, and mixing ratios:

$$\begin{aligned} & \frac{(\Phi_{\text{H}_2\text{O, evaporation}})(\chi_i/\chi_{\text{H}_2\text{O}})}{\text{kg s}^{-1} \text{ nonwater gas at ocean-plume interface}} \\ &= \frac{(\Phi_{\text{H}_2\text{O, eruption}})(\chi_{i, \text{Cassini}}/\chi_{\text{H}_2\text{O, Cassini}})}{\text{kg s}^{-1} \text{ nonwater gas at surface of Enceladus.}} \end{aligned} \quad (8)$$

Here, χ_i is the molar mixing ratio of each gas i just above the ocean–plume boundary, and $\chi_{i, \text{Cassini}}$ is the molar mixing ratio measured by the Cassini spacecraft in the plume above Enceladus (see Table 1). By mass conservation, the total mass flow rate (kg s^{-1}) of any gas at the surface of Enceladus is the same as at the Cassini spacecraft altitude. Consequently, in Equation (8), we take eruption rates at the surface of Enceladus as proportional to mixing ratios in the erupted plume as measured by Cassini. Also, in Equation (8), we assume that exsolution rates for nonwater gases from the ocean are proportional to their mixing ratios just above the ocean. For the mass flow rates of water, we assume that evaporation is proportional to the water vapor mixing ratio just above the ocean. Water vapor is lost to fissure walls, but although $\Phi_{\text{H}_2\text{O, evaporation}} > \Phi_{\text{H}_2\text{O, eruption}}$, this change in water mass flow is compensated for in Equation (8) by $\chi_i/\chi_{\text{H}_2\text{O}} < \chi_{i, \text{Cassini}}/\chi_{\text{H}_2\text{O, Cassini}}$, such that mass conservation of nonwater gases is expressed by the equality.

The definition of Equations (7)–(8) differs from the assumptions of Glein et al. (2015) and Glein & Waite (2020) where conservation was instead framed in terms of densities. We use mass flow rates (kg s^{-1}) in our definition because mass flow rate is conserved for flowing fluids in a conduit while density and velocity may vary. In the condensation model described in Section 2.1 (from Nakajima & Ingersoll 2016), the plume water vapor accelerates due to pressure gradients toward the surface and the vacuum of space. Nonwater gases will accelerate similarly, meaning that velocity may increase, density may decrease, but mass flow rate for the nonwater gases must be conserved throughout the fissure.

The statement of mass conservation in Equation (7) will not apply to water vapor due to loss via condensation, so instead we define a fractional loss of water vapor,

$$f_{\text{vapor loss}} = 1 - \frac{\Phi_{\text{H}_2\text{O, eruption}}}{\Phi_{\text{H}_2\text{O, evaporation}}}. \quad (9)$$

Here, $f_{\text{vapor loss}}$ is the fraction of plume water vapor lost via condensation onto the fissure walls. Again this definition deviates from the work of Glein et al. (2015) and Glein & Waite (2020) where vapor loss was defined by a change in the vapor density. We will explore the implications of this difference in Section 3.

By combining Equations (8)–(9) we can find molar mixing ratios directly above the ocean from known plume-measured mixing ratios and derived vapor loss from the condensation model,

$$\frac{\chi_i}{\chi_{\text{H}_2\text{O}}} = (1 - f_{\text{vapor loss}}) \frac{\chi_{i, \text{Cassini}}}{\chi_{\text{H}_2\text{O, Cassini}}}. \quad (10)$$

To find the partial pressures of all plume gases just above the ocean–plume interface, we use

$$p_i = \frac{\chi_i}{\chi_{\text{H}_2\text{O}}} p_{\text{H}_2\text{O}}. \quad (11)$$

Here, Equation (11) assumes that water vapor dominates the total pressure.

We additionally estimate how the salt concentration of ice grains may be altered by vapor condensation onto the grains. As described in Section 2.1, we find a ratio of surface areas for plume ice grains to fissure walls of $\sim 1:10^9$. For total condensation rates on the order of $\sim 10^2\text{--}10^3 \text{ kg s}^{-1}$ (Nakajima & Ingersoll 2016), and assuming condensation rates proportional to the surface areas of nucleation sites ($\Phi_{\text{cond., grains}}/\Phi_{\text{cond., walls}} = SA_{\text{grains}}/SA_{\text{walls}}$) we estimate condensations rates onto ice grains of $\sim 10^{-7}\text{--}10^{-6} \text{ kg s}^{-1}$. For total plume eruption rates $\sim 10^2 \text{ kg s}^{-1}$ (Hansen et al. 2017, 2020), the eruption rate of ice grains is $\sim 10 \text{ kg s}^{-1}$ (Hedman et al. 2018). Thus the fraction of the erupting ice grain mass that comes from condensed water vapor is only $10^{-8}\text{--}10^{-7}$. Because of this minimal contribution of condensed water vapor to the mass of ice grains, the salt concentrations of these grains measured by the CDA are taken as equal to salt concentrations in the ocean.

2.3. Models of Ocean Degassing

In order to find the abundances of dissolved gases in the ocean, we require a model of mass transfer across the ocean–plume phase boundary. Due to considerable uncertainty in the mechanisms by which the plume gas is produced, we outline three potential models for ocean outgassing (see Figure 2) in the following subsections: (1) a thin-film model of mass transfer from the ocean surface; (2) a boiling model where gases exsolve into vapor bubbles as they rise from a boiling depth < 1 meter (Ingersoll & Nakajima 2016) below the ocean surface; and (3) a model proposed by Glein & Waite (2020) wherein the plume gas flux is dominated by degassing of aerosol-like droplets.

2.3.1. Thin-film Gas Exsolution Model

First, we adopt a thin-film model of mass transfer to describe gas exsolution (Figure 2(a)), wherein mass transfer across the phase boundary is limited by diffusion through a hypothetical interfacial film at the ocean surface that is stagnant, i.e., not convecting (Cussler 2009). Thin-film models have also been applied to gas exsolution from the terrestrial ocean (Broecker & Peng 1982). The molar flux across this liquid–gas boundary (where ocean transitions to plume) for each gas species, i , is given by the following equation,

$$J_i = K_{p,i}(p_i^* - p_i). \quad (12)$$

Here, $K_{p,i}$ is an overall mass-transfer coefficient (in units of $\text{mol m}^{-2} \text{ Pa}^{-1} \text{ s}^{-1}$), p_i^* is a theoretical gas partial pressure that would be in equilibrium with the concentration in the ocean (related via Henry’s law: $p_i^* = x_i/H_i$), and p_i is the actual partial pressure in the plume gas just above the phase boundary. Overall mass-transfer coefficients for the dissolved gases ($K_{p,i}$)

are found via

$$\frac{1}{K_{p,i}} = \frac{1}{k_{x,i}H_i} + \frac{1}{k_{p,i}} \approx \frac{1}{k_{x,i}H_i}. \quad (13)$$

Here, H_i is the Henry’s law coefficient for gas i (in units of Pa^{-1} ; Sander 2015), $k_{x,i}$ is the liquid-sided mass-transfer coefficient (in units of $\text{mol m}^{-2} \text{ s}^{-1}$), and $k_{p,i}$ is the gas-sided mass-transfer coefficient (in units of $\text{mol m}^{-2} \text{ Pa}^{-1} \text{ s}^{-1}$). Henry’s law and mass-transfer coefficients vary significantly between gases. The liquid-sided mass-transfer coefficient can be related to a diffusion coefficient via

$$k_{x,i} = \frac{D_i c_{\text{H}_2\text{O}}}{\Delta}. \quad (14)$$

Here, D_i (in units of $\text{m}^2 \text{ s}^{-1}$) is the diffusion coefficient through liquid water, $c_{\text{H}_2\text{O}}$ is the concentration of water ($\approx 5.55 \times 10^4 \text{ mol m}^{-3}$), and Δ is the thickness of the interfacial thin film, often taken as 0.0001 m (Cussler 2009). The approximation in Equation (13) can be made because for most gases the diffusion coefficient through water vapor is much larger than the diffusion coefficient through liquid water, and therefore $k_{p,i} \gg k_{x,i}$. In other words, the slower diffusion through the liquid dominates the overall mass-transfer rate, effectively acting as a bottleneck.

As introduced in Equation (5), we adopt the Hertz relation to model evaporation from the ocean. We can define a mass-transfer coefficient for water in the same units as the overall mass-transfer coefficients for dissolved gases ($\text{mol m}^{-2} \text{ Pa}^{-1} \text{ s}^{-1}$) via

$$K_{p,\text{H}_2\text{O}} = \frac{1}{\sqrt{2\pi RTM}}. \quad (15)$$

Here, as in Equation (5), R is the ideal gas constant, T is the temperature at the ocean–plume interface, and M is the molar mass of water.

To determine concentrations of gases in the ocean, we assume that the partial pressures of all gases directly above the ocean are proportional to their molar fluxes across the ocean–plume boundary (as defined in Equation (12)), e.g., for a nonwater gas species i relative to water,

$$\frac{p_i}{p_{\text{H}_2\text{O}}} = \frac{J_i}{J_{\text{H}_2\text{O}}} = \frac{K_{p,i}(p_i^* - p_i)}{K_{p,\text{H}_2\text{O}}(\Delta p_{\text{H}_2\text{O}})}. \quad (16)$$

Here, $\Delta p_{\text{H}_2\text{O}}$ is the difference between the saturation vapor pressure of the liquid and the partial pressure of water in the vapor phase. Also, p_i^* is as defined after Equation (12). Rearranging the above equation, we solve for the partial pressure of gas i in the ocean,

$$p_i^* = p_i + \frac{p_i K_{p,\text{H}_2\text{O}}(\Delta p_{\text{H}_2\text{O}})}{p_{\text{H}_2\text{O}} K_{p,i}}. \quad (17)$$

Finally, to convert hypothetical partial pressures to molal concentrations (moles per kilogram of H_2O), we use

$$b_i = \frac{p_i^* H_i}{M}. \quad (18)$$

Here, b_i is the molality of species i , H_i is the Henry’s law constant in units of Pa^{-1} , and M is the molar mass of water.

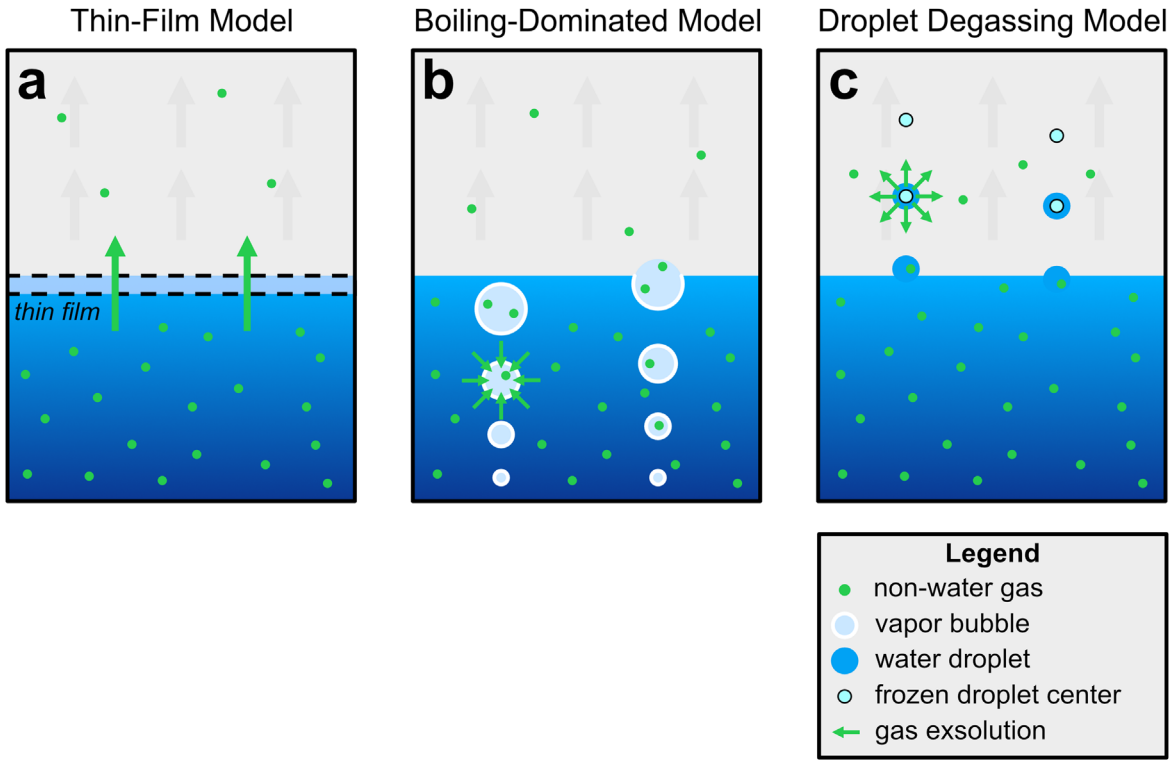


Figure 2. The three models of ocean outgassing considered in this study. (a) In a thin-film gas exsolution model, outgassing fluxes from the ocean are determined by diffusive mass transfer across a hypothetical stagnant (i.e., not convecting) thin film at the ocean–gas interface. (b) In a boiling-dominated model, gases exsolve into vapor bubbles that rise and grow from a boiling depth ~ 0.71 m below the surface (Ingersoll & Nakajima 2016). The relative gas abundances in the plume are then set by the gas abundances acquired during the bubbles’ short (< 5 s) journey to the surface. (c) In a droplet-dominated degassing model (Glein & Waite 2020), gas in the plume is the result of complete vaporization of the outer layer of aerosol-like water droplets, while the inner volume of the droplets freeze and form ice grains of the plume.

2.3.2. Boiling Vapor Bubble Model

In the second outgassing scenario, we consider a case where the release of gas from Enceladus’ ocean is dominated by vapor bubbles produced by ocean boiling under near-vacuum conditions (Figure 2(b)). We take the boiling depth of 0.71 m calculated by Ingersoll & Nakajima (2016) as the depth from which these bubbles originate. As the bubbles rise due to buoyant forces, water vapor and nonwater gases alike exsolve into the bubble. The degree to which the partial pressures of gases in the bubble equilibrate with the ocean is directly proportional to their rates of exsolution. However, unlike the thin-film model of exsolution at the surface, in the boiling scenario the gas phase (the bubble) has some time to at least partially equilibrate before it reaches the surface.

To estimate the growth of rising vapor bubbles, we adopt Rayleigh’s (1917) model for spherical bubble growth:

$$\frac{dR_{\text{bubble}}}{dt} = \pm \sqrt{\frac{2}{3} \left(\frac{P_{\text{sat}}(T_{\infty}) - P_{\infty}}{\rho_l} \right)}. \quad (19)$$

Here, R_{bubble} is the radius of the spherical bubble, $P_{\text{sat}}(T_{\infty})$ is the saturation vapor pressure of the liquid at the far-field temperature T_{∞} (i.e., the temperature of the liquid), P_{∞} is the far-field (i.e., the hydrostatic) pressure, and ρ_l is the density of the liquid. We include a thermal lapse rate of -2.70 K m^{-1} in this near-surface layer as determined by Ingersoll & Nakajima (2016), so that T_{∞} is a function of depth.

To estimate the velocity of the rising vapor bubbles, we use Park et al.’s (2017) parameterization for the size-dependent

velocity (v_b) of vapor bubbles,

$$v_b = \frac{1}{\sqrt{\frac{144\mu_l^2}{g^2\rho_l^2d_e^4} + \frac{\mu_l^{4/3}}{0.14425^2g^{5/3}\rho_l^{4/3}d_e^3} + \frac{1}{\frac{2.14\sigma_l}{\rho_l d_e} + 0.505gd_e}}}. \quad (20)$$

Here, μ_l is the viscosity of the liquid, g is gravitational acceleration, d_e is the equivalent diameter of the bubble (in the simplified spherical model we consider, $d_e = 2R_{\text{bubble}}$ always), and σ_l is the surface tension of the liquid. While Equation (20) includes terms that describe how bubble velocity changes with shape (as large bubbles change from spheres to spherical caps; Park et al. 2017), we approximate all bubbles as spherical regardless of size, for simplicity in calculating their surface areas and volumes.

Rates of gas transfer from the dissolved aqueous phase into the bubble are found by

$$\begin{aligned} \frac{dn_i}{dt} &= K_{p,i}(p_i^* - p_{i,\text{bubble}}(t))A_{\text{bubble}}(t) \\ &= K_{p,i}(p_i^* - p_{i,\text{bubble}}(t))4\pi(R_{\text{bubble}}(t))^2. \end{aligned} \quad (21)$$

Here, n_i is the total number of moles of gas i in the bubble, $K_{p,i}$ is once again an overall mass-transfer coefficient in units of $\text{mol m}^{-2} \text{ s}^{-1} \text{ Pa}^{-1}$, p_i^* is the partial pressure of gas i in the ocean, $p_{i,\text{bubble}}$ is the partial pressure in the bubble, A_{bubble} is the surface area of the bubble, and R_{bubble} is the bubble radius. The changing partial pressure in the bubble is found using the

ideal gas law ($p_{i,\text{bubble}}V_{\text{bubble}} = n_iRT_{\infty}$),

$$\begin{aligned} \frac{dp_{i,\text{bubble}}}{dt} &= K_{p,i}(p_i^* - p_{i,\text{bubble}}(t))A_{\text{bubble}}(t) \frac{RT_{\infty}}{V_{\text{bubble}}(t)} \\ &= K_{p,i}(p_i^* - p_{i,\text{bubble}}(t)) \frac{3RT_{\infty}}{R_{\text{bubble}}(t)}. \end{aligned} \quad (22)$$

Here, R is the ideal gas constant, V_{bubble} is the volume of the spherical bubble, and we have assumed that the bubble is in thermal equilibrium with the ocean such that T_{∞} can be taken as the temperature of gas.

We use two different methods to determine mass-transfer coefficients for gas transfer into the bubble. The first comes from Higbie (1935), as cited in Nock et al. (2016), where a mass-transfer coefficient (in units of meters per second) is defined by

$$k_{L,i} = 2 \sqrt{\frac{D_i v_b}{\pi d_e}}. \quad (23)$$

Here, D_i is the diffusion coefficient of gas i in water. The second formulation we use for the mass-transfer coefficient comes from Frössling (1938), as cited in Nock et al. (2016),

$$k_{L,i} = c \sqrt{\frac{v_b}{d_e}} D_i^{(2/3)} \nu_l^{(-1/6)}. \quad (24)$$

Here, c is a unitless coefficient that varies from 0.42–0.95 (Nock et al. 2016) and ν_l is the kinematic viscosity ($= \mu/\rho_l$). The mass-transfer coefficients defined in Equations (23) and (24) are converted into overall mass-transfer coefficients (Cussler 2009) via

$$K_{p,i} = k_{x,i}H_i = k_{L,i}c_{\text{H}_2\text{O}}H_i. \quad (25)$$

Here, as in the thin-film model definition in Section 2.3.1, $k_{x,i}$ is the liquid-sided mass-transfer coefficient, $c_{\text{H}_2\text{O}}$ is the concentration of water, and H_i is the Henry’s law constant in units of Pa^{-1} .

We take the two definitions for mass-transfer coefficients from Equations (23) and (24) as conservative upper and lower limits for the rate of gas transfer, noting that experimentally measured gas transfer rates of CO_2 into bubbles fall within this range (Nock et al. 2016). Because Equation (24) (Frössling 1938) provides the lower of the two estimates, we adopt the lowest value for c ($= 0.42$) to find the most conservative lower limit for this mass-transfer coefficient. We also note that an overall mass-transfer coefficient calculated using the thin-film model of Section 2.3.1 (using Equations (13) and (14)) falls within the the limits provided by Equations (23) and (25) or (24) and (25), so the possibility that thin-film diffusion governs gas transfer into the bubbles is implicitly included in this boiling vapor bubble model.

To derive oceanic gas concentrations from plume ratios in the case of boiling-dominated outgassing, we must define a relationship between the partial pressures of gases above the ocean, and the partial pressures that would be in equilibrium with ocean concentrations. To accomplish this, we numerically model a bubble growing and rising from an initial depth ranging from $z = -0.71$ to -0.01 m, with initial zero bubble radius and zero bubble velocity. We use this range for initial depth because bubbles can nucleate at any depth within the boiling layer. We step forward in time with a finite-difference method, using Equation (19) to find the bubble’s growing radius (and, in turn, the spherical bubble’s surface area and

volume), and Equation (20) to find the bubble’s velocity (and, in turn, the bubble’s vertical position z). During this rising and growing period, we find the changing partial pressures of H_2 , CO_2 , CH_4 , and NH_3 in the bubble using Equation (22). When the bubble reaches the ocean surface ($z = 0$), we stop the model and note the ratio between the final partial pressure in the bubble ($p_{i,\text{bubble,final}}$) and the hypothetical partial pressure in equilibrium with the aqueous phase (p_i^*),

$$f_{i,\text{boiling}} = \frac{p_{i,\text{bubble,final}}}{p_i^*}. \quad (26)$$

We assume that in the boiling-dominated outgassing model, the partial pressures in the bubble upon reaching the surface are equivalent to the partial pressures just above the ocean ($p_{i,\text{bubble,final}} = p_i$). Thus combining Equations (18) and (26), we find the molality of dissolved gases in the boiling-dominated scenario to be

$$b_i = \frac{p_i}{f_{i,\text{boiling}}M} \frac{H_i}{M}. \quad (27)$$

Here p_i is the partial pressure of gas i just above the ocean (an output of the condensation model; Equation (11)), H_i is the Henry’s law constant, and M is the molar mass of water.

Bubbles tend to nucleate in cavities on surfaces (in this case, e.g., cavities in the submerged portion of the fissure walls), growing to some “departure diameter” at which point upward forces on the bubble (e.g., buoyancy) overcome downward forces (e.g., surface tension), and the bubble detaches from the nucleation site (Jones et al. 1999). In the case of the Enceladus ocean–plume system, the initial stage of bubble growth before detachment could increase the final bubble volume and thus decrease the final partial pressure in the bubble and $f_{i,\text{boiling}}$ (Equation (26)). To include this effect, we calculate the departure diameter from a semiempirical formula (Kocamus-tafaogullari 1983)

$$d_d = 2.64 \times 10^{-5} \left(\frac{\sigma_l}{g\Delta\rho} \right)^{0.5} \text{me} \left(\frac{\Delta\rho}{\rho_g} \right)^{0.9}. \quad (28)$$

Here, σ_l is the surface tension of the liquid, g is the gravitational acceleration, $\Delta\rho$ is the density difference between the fluid and the vapor in the bubble, and ρ_g is the density of the vapor in the bubble. For the initial stationary period of bubble growth, we use the time derivative of the expanding bubble radius (Equation (19)) in place of the bubble’s translational velocity when calculating mass-transfer rates from Equations (23) and (24).

2.3.3. Aerosol Droplet Degassing Model

Previous work by Glein & Waite (2020) assumed a model where gas transfer into the plume occurs primarily from aerosol-like droplets of ocean spray (Figure 2(c)). That study posited that due to rapid freezing of these droplets and formation of an ice shell in the inner volume (Waite et al. 2017), degassing and evaporation should only occur from the outermost layer of the droplet. Complete degassing of this outer layer would imply equal abundances between the ocean and plume gas concentrations (Glein & Waite 2020). In this model

plume abundances can be related to ocean abundances via

$$\left(\frac{\chi_i}{\chi_{\text{H}_2\text{O}}} \right)_{\text{plume at ocean}} = \left(\frac{\chi_i}{\chi_{\text{H}_2\text{O}}} \right)_{\text{in ocean}} \quad \text{or} \quad b_i = \frac{p_i}{p_{\text{H}_2\text{O}}M}. \quad (29)$$

Here, b_i is the molality of gas i in the ocean (mol kg^{-1} water), p_i and $p_{\text{H}_2\text{O}}$ are the partial pressures (Pa) just above the ocean of gas i and water vapor, respectively, and M is the molar mass of water (kg mol^{-1}). We will compare the outputs of this and the other two ocean degassing models in Section 3.

2.4. Aqueous Chemistry Model

The physical chemistry models in Sections 2.1, 2.2, and 2.3 provide a method to estimate dissolved gas concentrations in the ocean from plume measurements; additionally modeling aqueous chemistry allows us to estimate the ocean pH and concentrations of dissolved ions. In aqueous chemistry, there is charge balance, such that the total oceanic concentration of positively charged cations is equal to the total concentration of negatively charged anions. CDA analysis of the solid ice grains suggests that the dominant salts in Enceladus' ocean are NaCl and NaHCO₃ or Na₂CO₃. The salinities in the ice grains ($[\text{NaCl}] = 0.05\text{--}0.2$ molal, $[\text{Na}_2\text{CO}_3$ or $\text{NaHCO}_3] = 0.01\text{--}0.1$ molal) are thought to closely represent the ocean salinity (Postberg et al. 2009; see also Section 2.2). Our charge balance equation includes the concentrations of the ionic components of these salts (Na^+ , Cl^- , HCO_3^- , CO_3^{2-}), the dissociation products of water (H^+ and OH^-), and the dissolved NH₃ speciation product ammonium (NH_4^+):

$$[\text{Na}^+] + [\text{NH}_4^+] + [\text{H}^+] = [\text{Cl}^-] + [\text{HCO}_3^-] + 2[\text{CO}_3^{2-}] + [\text{OH}^-]. \quad (30)$$

Here, the brackets indicate the molal concentration of the ion. To solve the above equation, due to the pH-dependent speciation of carbonates and ammonia and dissociation of water, we can rewrite many of the above species in terms of $[\text{H}^+]$ (related to the pH), equilibrium constants, and activity coefficients (γ_i). We rearrange to put known quantities on the left side:

$$\begin{aligned} [\text{Na}^+] - [\text{Cl}^-] &= [\text{HCO}_3^-] + 2[\text{CO}_3^{2-}] \\ &+ [\text{OH}^-] - [\text{H}^+] - [\text{NH}_4^+] \\ &= \frac{K_1\gamma_{\text{CO}_2}[\text{CO}_2^*]}{\gamma_{\text{HCO}_3^-}\gamma_{\text{H}^+}[\text{H}^+]} + 2\frac{K_1K_2\gamma_{\text{CO}_2}[\text{CO}_2^*]}{\gamma_{\text{CO}_3^{2-}}(\gamma_{\text{H}^+})^2[\text{H}^+]^2} \\ &+ \frac{K_w a_w}{\gamma_{\text{OH}^-}\gamma_{\text{H}^+}[\text{H}^+]} - [\text{H}^+] - \frac{[\text{NH}_3]\gamma_{\text{H}^+}[\text{H}^+]}{\gamma_{\text{NH}_4^+}K_a}. \end{aligned} \quad (31)$$

Here, $[\text{CO}_2^*]$ ($\approx[\text{CO}_2]$) is the total concentration of dissolved CO₂ and carbonic acid (H_2CO_3), K_1 is the dissociation constant of carbonic acid into bicarbonate, K_2 is the dissociation constant of bicarbonate into carbonate, K_w is the dissociation constant for water, and K_a is the dissociation constant of NH_4^+ into NH₃. To find these temperature-dependent constants at the estimated ocean temperature of 273 K, we use experimentally determined values and equations developed to match empirical data (Bates & Pinching 1949; Millero et al. 2002; Bandura & Lvov 2006). In Equation (31), γ_i refers to the activity

coefficient of a species i , and a_w is the activity of water (see Appendix B for full calculation of activity coefficients and a_w).

By noting that the bulk of sodium ions are those associated with NaCl and Na-carbonate salts, we can assume the following:

$$[\text{Na}^+] = [\text{Na}^+]_{\text{NaCl}} + [\text{Na}^+]_{\text{Na-carbonates}}, \quad (32)$$

$$[\text{Cl}^-] = [\text{Cl}^-]_{\text{NaCl}}. \quad (33)$$

Since $[\text{Na}^+]_{\text{NaCl}} = [\text{Cl}^-]_{\text{NaCl}}$, Equation (31) can be simplified to

$$\begin{aligned} [\text{Na}^+]_{\text{Na-carbonates}} &= \frac{K_1\gamma_{\text{CO}_2}[\text{CO}_2^*]}{\gamma_{\text{HCO}_3^-}\gamma_{\text{H}^+}[\text{H}^+]} + 2\frac{K_1K_2\gamma_{\text{CO}_2}[\text{CO}_2^*]}{\gamma_{\text{CO}_3^{2-}}(\gamma_{\text{H}^+})^2[\text{H}^+]^2} \\ &+ \frac{K_w a_w}{\gamma_{\text{OH}^-}\gamma_{\text{H}^+}[\text{H}^+]} - [\text{H}^+] \\ &- \frac{[\text{NH}_3]\gamma_{\text{H}^+}[\text{H}^+]}{\gamma_{\text{NH}_4^+}K_a}. \end{aligned} \quad (34)$$

Using $[\text{Na}^+]_{\text{Na-carbonates}} = 0.01\text{--}0.1$ molal, and approximating $[\text{CO}_2^*]$ as $[\text{CO}_2]$ (a quantity we have derived via the fractionation model), we solve the above equation numerically for $[\text{H}^+]$. Once $[\text{H}^+]$ is known, pH ($=-\log(\gamma_{\text{H}^+}[\text{H}^+])$) and $[\text{NH}_4^+]$ ($=[\text{NH}_3]\gamma_{\text{H}^+}[\text{H}^+]/\gamma_{\text{NH}_4^+}K_a$) are derived for the ocean. We initially assume that all activity coefficients are equal to 1 to get a rough estimate for the concentrations of all unknown ionic species ($[\text{NH}_4^+]$, $[\text{CO}_3^{2-}]$, $[\text{HCO}_3^-]$, $[\text{H}^+]$, and $[\text{OH}^-]$). We then follow the Pitzer method (described in Appendix B) to find the activity coefficients for ions and the activity of water. We plug these activity coefficients and the activity of water into Equation (34) and iteratively repeat until our numerical solutions for dissolved concentrations converge.

2.5. Implications for Possible Methanogenesis

Finally, we explore the available energy for hydrogenotrophic methanogenesis in the ocean, from the H₂-CO₂ redox pair. Following the method of Waite et al. (2017), we calculate an ‘‘apparent affinity,’’ a measure of the available energy for the H₂-CO₂ redox pair in the ocean, via

$$A = 2.302 \, 6RT (\log K - \log Q), \quad (35)$$

where R is the universal gas constant, T is the temperature of the medium, K is the equilibrium constant for the reaction, and Q is the reaction quotient. As in Waite et al. (2017), $\log K$ is taken to be 37.44, while $\log Q$ is defined based on the predicted dissolved gas concentrations via

$$\log Q = \log \left(\frac{[\text{CH}_4][\text{H}_2\text{O}]^2}{[\text{CO}_2][\text{H}_2]^4} \right), \quad (36)$$

from the chemical equation $\text{CO}_2 + 4\text{H}_2 \rightleftharpoons \text{CH}_4 + 2\text{H}_2\text{O}$.

3. Results

We ran our model for a range of fissure geometries, with depths from 1000–5000 m, outlet diameters from 0.05–0.1 m, fissure diameters at the ocean interface from 0.05–1000 m, and tapering factors from 1–100 m, and made predictions for dissolved gas concentrations, ion concentrations, and ocean pH for each geometry. We found that narrower fissures or

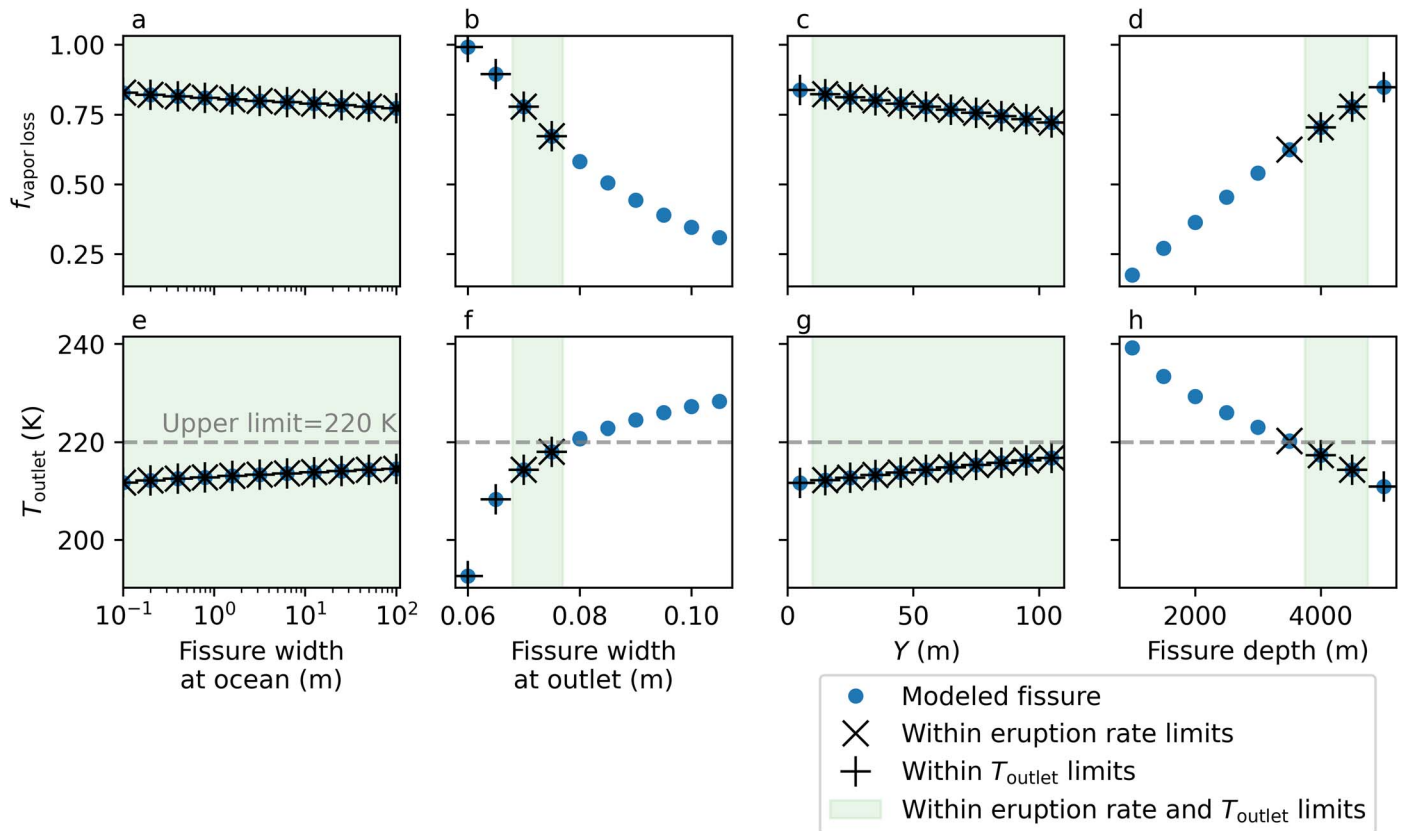


Figure 3. A subset of our modeling results to show the effect of fissure geometry on condensation. Top row: the fraction of plume vapor loss (a model output, defined in Equation (9)) that occurs due to condensation for different fissure geometries (model inputs), varying (a) fissure width at the ocean–plume interface, (b) fissure width at the plume outlet, (c) the tapering factor Y (see Equation (6)), and (d) the depth of the fissure from outlet to ocean–plume interface. Bottom row: the temperature of the ice walls at the fissure outlet (a model output) for different fissure geometries varying (e) fissure width at the ocean–plume interface, (f) fissure width at the plume outlet, (g) the tapering factor Y , and (h) the depth of the fissure from outlet to ocean–plume interface. In all subplots shown here, the fissure’s geometrical parameters are held constant at the following values unless varied on the x -axis: $\delta_0 = 50$ m, $\delta_{\text{outlet}} = 0.07$ m, $Y = 55$ m, $D = 4500$ m. Blue points indicate unrestricted model results, points with black “ \times ”s are models that reproduce observed eruption rates of $180\text{--}338$ kg s^{-1} (Hansen et al. 2017, 2020), and models with black “+”s produce fissure outlet temperatures ≤ 220 K (the gray dashed line in the bottom row also indicates this temperature limit). Only fissures that fit both restrictions (points with “ \times ” and “+”, also indicated by the shaded region) are deemed viable. Fissures that are narrower at the outlet or deeper overall result in a larger fraction of the plume’s water vapor being removed (b) and (d)), and thus will produce larger differences between relative gas abundances in the plume at the bottom of the conduit versus at the top (at Enceladus’ surface). Fissures that are narrower at the ocean interface or have a smaller tapering factor Y also tend to lose more water vapor ((a) and (c)), but the effect is less pronounced. Across all plots, T_{outlet} is anticorrelated with the fraction of water vapor lost, because the final vapor pressure of the plume is tied directly to the temperature of the ice wall at the outlet (Equation (4)).

deeper fissures (where the plume has a longer distance to travel from ocean to fissure outlet) tend to result in lower predicted oceanic gas concentrations. This comes from the fact that narrower and/or deeper fissures tend to lose more water vapor via condensation (Figure 3). Therefore direct measurements of the erupted plume and lack of accounting for condensation would severely *overestimate* the concentrations of the minor (i.e., nonwater) gases in these cases. In the case of a wider and/or shallower fissure, water loss via condensation is lower so the discrepancies between plume and ocean abundances are smaller, resulting in higher predicted dissolved gas concentrations. The fractional loss of water vapor may also be understood in terms of the fissure wall’s temperature: wider outlets and shallower fissures correspond to higher fissure outlet temperatures (Figure 3) and therefore smaller temperature differences between ocean and outlet. Because the vapor pressure of the plume is temperature dependent and set by rapid equilibration with the fissure walls (Equation (4)), a smaller temperature change over the eruptive journey results in less vapor lost. Fissures with narrower widths at the ocean interface and smaller tapering factors also tend to result in greater vapor loss (Figures 3(a), (c)), but the influence of these two

parameters is less significant than for fissure outlet width and fissure depth (Figures 3(b), (d)) over the range of geometries considered.

We can constrain our predictions for ocean gas concentrations based on observed eruption rates, observed outlet temperature constraints, and reasonable upper limits on ion concentrations from plume ice grain composition. We first narrow our consideration of fissure geometries to only those that reproduce observed eruption rates of $180\text{--}338$ kg s^{-1} total plume mass (Hansen et al. 2017, 2020). We follow the example of Nakajima & Ingersoll (2016) in using this constraint, considering only fissure geometries where the erupted flux times the fissure diameter, times the total length of the fissure (taken to be $1\text{--}1.7 \times 500$ km) are within the uncertainty range of $180\text{--}338$ kg s^{-1} . We also restrict our predictions based on the temperature of the ice at the plume outlet—an output parameter of the vapor condensation model. We only consider fissure models with outlet temperatures ≤ 220 K, on the basis that fissures at temperatures exceeding this should sublimate away meters of ice within days, widening the fissure outlet, and rapidly exposing colder ice at greater depth and distance away from the outlet (Goguen et al. 2013). Finally, we set an upper

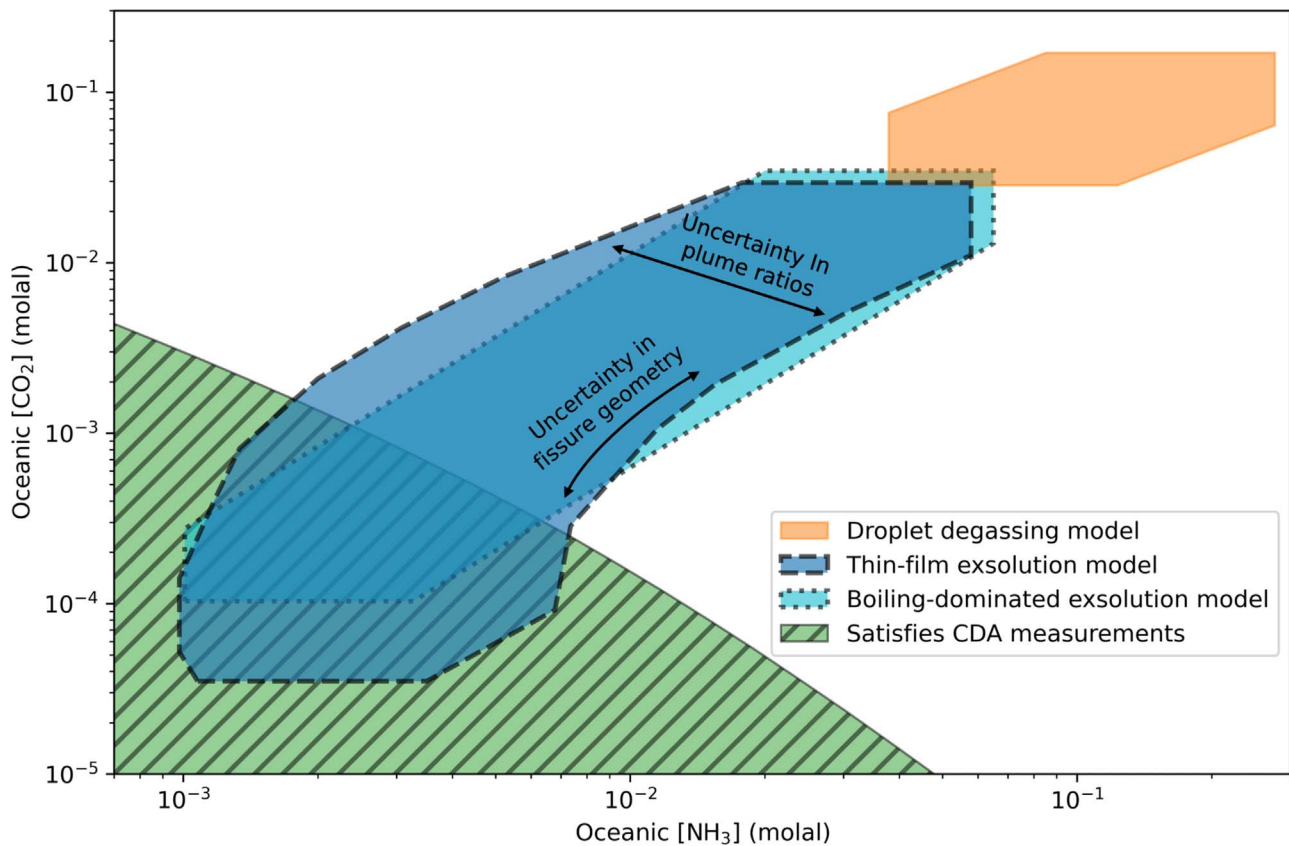


Figure 4. Model predictions for dissolved concentrations of NH_3 (horizontal axis) and CO_2 (vertical axis). The flat-color regions (dark blue, cyan, orange) show the range of oceanic dissolved gas predictions for each outgassing model (thin-film exsolution, boiling-dominated exsolution, and droplet degassing, respectively). For each model, the full range of predictions includes uncertainty from both the range of fissure geometries that reproduce observed eruption rates of $180\text{--}338\text{ kg s}^{-1}$ (Hansen et al. 2017, 2020) and produce fissure outlet temperatures $\leq 220\text{ K}$, and uncertainty in the plume measurements of gas mixing ratios (Waite et al. 2017; see Table 1). Generally the extent of each of the three regions from upper left to lower right corresponds to uncertainty in the plume mixing ratios, while the extent from lower left to upper right corresponds to uncertainty from the range of fissure geometries that match observations (both directions are indicated with labeled black arrows). The striped green region indicates the combination of CO_2 and NH_3 concentrations that are reconcilable with CDA measurements of salts; that is, $[\text{NaCl}] = 0.05\text{--}0.2\text{ molal}$, $[\text{Na}_2\text{CO}_3\text{ or NaHCO}_3] = 0.01\text{--}0.1\text{ molal}$ (Postberg et al. 2009), and all ion concentrations $\leq 0.2\text{ molal}$. The region of overlap between the striped green region and any of the other regions shows the range of predictions for a given outgassing model that is compatible with CDA measurements. The thin-film exsolution model produces the largest range in possible oceanic concentrations, the boiling-dominated exsolution model has a smaller range with similar upper limits, and the droplet degassing model does not produce any chemistries that are reconcilable with CDA measurements.

limit on ion concentrations predicted by the aqueous chemistry model. Although upper limits of ammonium ions in plume ice grains (and therefore the ocean) have not yet been defined in analysis of CDA data, if we assume comparable instrument sensitivity between NH_4^+ salts and salts that were measured (e.g., NaCl), we can set an estimated upper limit for all ions of 0.2 molal water (based on the upper limit established for NaCl ; Postberg et al. 2009).

The three restrictions described above (eruption rate, T_{outlet} , and ion chemistry) reduce the uncertainty in our dissolved gas concentrations to within 2–3 orders of magnitude (Figures 4, 5). Generally we predict fairly high gas concentrations in the ocean, with concentrations of $\sim 10^{-5}\text{--}10^{-3}\text{ molal}$ (Figure 5). Specifically, we find the following molal concentrations: $[\text{CO}_2] = 3.5 \times 10^{-5}$ to 1.8×10^{-3} , $[\text{CH}_4] = 1.1 \times 10^{-5}$ to 6.4×10^{-4} , $[\text{H}_2] = 1.4 \times 10^{-5}$ to 9.3×10^{-4} , and $[\text{NH}_3] = 9.8 \times 10^{-4}$ to $7.2 \times 10^{-3}\text{ molal}$. Using the aqueous chemistry model described in Section 2.4, we obtain concentrations of ammonium ions in the ocean between 0.01 and 0.2 molal (Figure 5). Notably all fissures with widths $< \sim 5\text{ m}$ at the ocean-plume interface (not included in Figures 4 and 5) are ruled out of our predictions for the ocean chemistry because they lead to very high ($> 1\text{ molal}$) concentrations of gases. Such

high molalities of neutral dissolved gases like CO_2 and NH_3 further imply ion concentrations of $10\text{--}1000\text{ molal}$, which would be extremely difficult to reconcile with ice grain compositions that are $> 98\%$ water (Postberg et al. 2009), or solubility limits on the order of $1\text{--}10\text{ molal}$.

We also find that the droplet-dominated degassing model produces high gas concentrations ($\sim 10^{-1}\text{ molal}$), and consequently ion concentrations of $10^0\text{--}10^2\text{ molal}$ (orange region in Figure 4) that are irreconcilable with CDA measurements. This result contrasts with the findings of Glein & Waite (2020), where a droplet-dominated degassing model predicted CO_2 concentrations of $\sim 10^{-6}\text{--}10^{-3}\text{ molal}$ (red error bar in Figure 5). We predict gas concentrations several orders of magnitude higher (in the droplet-dominated case) because of the difference in how we handle mass conservation during vapor condensation. In our model, we find that the initial mixing ratios of nonwater gases in the plume are lower than what was measured by Cassini, by a factor of $(1 - f_{\text{vapor loss}})$ (Equation (10)), where $f_{\text{vapor loss}}$ is a fractional loss defined by eruption rates, and is on the order of $0.6\text{--}0.7$ (see Figure 3). By contrast, models where mass conservation and $f_{\text{vapor loss}}$ are defined in terms of equilibrium vapor densities would generally

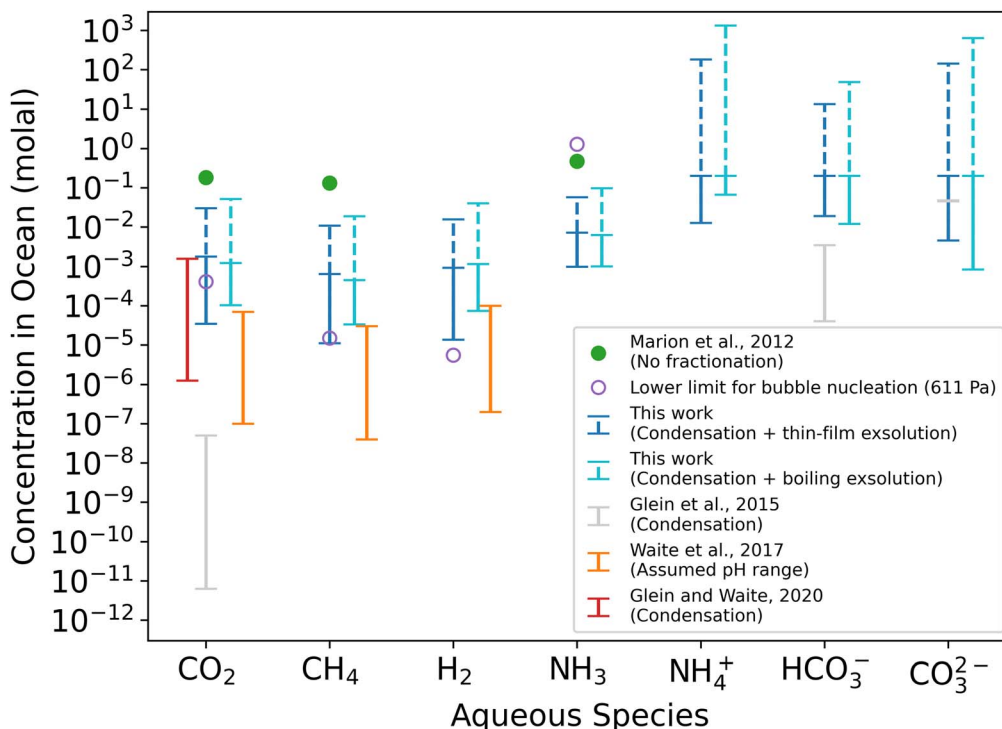


Figure 5. Predicted gas and ion concentrations from this work, using the thin-film model of exsolution (shown with dark blue error bars) and the boiling-dominated model of exsolution (cyan error bars) compared to previous studies. The two estimates from this work are shown as solid error bars for limits that are consistent with CDA analysis of salt content, while the dashed parts of the error bars are not consistent due to ion concentrations greater than 0.2 molal. Marion et al. (2012; green dots) assumed no fractionation between the plume and ocean. Waite et al. (2017; orange error bars) assumed a pH range of 9–11 based on prior studies, and found a CO_2 concentration that was consistent with that pH. They then used gas-to-gas ratios in the plume to find gas-to-gas ratios in the ocean. Glein et al. (2015; gray error bars) accounted for water vapor loss during condensation for a plume that stays in vapor pressure equilibrium with fissure walls that cool toward the surface. Glein & Waite (2020; red error bar) later reported an updated range for oceanic CO_2 using the same model of condensation as Glein et al. (2015) and additionally incorporating limits based on CDA measurements of salts. The open purple circles show the lowest concentration at which each gas would spontaneously form bubbles, as in a carbonated drink (Liger-Belair 2012). A limit for bubble nucleation that is below the estimates for gas concentration (seen for H_2) suggests that H_2 bubbles are likely forming in the near-surface ocean. NH_3 bubbles will not form because the required limit for bubble nucleation is far above the estimated oceanic concentrations.

find $f_{\text{vapor loss}} > 0.995$, and therefore much lower initial mixing ratios in the plume.

The concentrations of ammonium and ammonia calculated specifically for the droplet degassing model here may be overestimates because our model does not account for the dissociation kinetics of ammonium. Rapid dissociation of NH_4^+ into NH_3 (Perrin & Engler 1991) within liquid water aerosol droplets could occur simultaneously with droplet degassing of NH_3 , meaning that NH_3 in the plume could be sourced from a combination of both ammoniacal species (rather than NH_3 alone, which is the assumption of all our outgassing models). The most extreme endmember case would be complete conversion of dissolved NH_4^+ in the outer volume of the droplet into gaseous NH_3 , which would lead to predicted oceanic concentrations of total ammoniacal species ($\approx[\text{NH}_4^+]$ in the estimated pH regime) of 4×10^{-2} – 3×10^{-1} molal, and therefore $[\text{NH}_3] \approx 10^{-3}$ – 10^{-2} molal. These concentrations are more similar to the estimates of the thin-film and boiling-dominated models, but our predicted CO_2 concentrations would be unchanged (from the orange region in Figure 4), so we would still find no overlap between the droplet degassing model and the allowable chemistries from CDA analysis shown in Figure 4. Waite et al. (2017, Supplementary Material) found that speciation between CO_2 , CO_3^{2-} , and HCO_3^- is negligible on the timescales of droplet degassing and freezing, so CO_2 is not affected in the same way as NH_3 . We do not expect ammonium dissociation to affect predictions for aqueous ammonia in the thin-film model. Studies of ammonia

volatilization in the context of agricultural environments find that volatilization rates are predicted by thin-film models and are controlled by aqueous NH_3 , not directly by NH_4^+ or total ammoniacal concentrations (Jayaweera & Mikkelsen 1990; Jayaweera et al. 1990; Montes et al. 2009).

Using our predictions for dissolved gas concentrations and the equilibrium model of aqueous chemistry, we also model a pH range for the ocean. When limiting our results to fissure geometries that reproduce the observed rates of eruption, outlet temperatures, and our estimated upper limit for $[\text{NH}_4^+]$ (Figure 4), we predict a pH range of 7.95–9.05 (Figure 6). In addition to pH variation from different fissure geometries, a large contribution to uncertainty in our predicted ocean pH stems from uncertainties in the mixing ratios of CO_2 and NH_3 in the erupted plume, 0.3–0.8 and 0.4–1.3, respectively (Waite et al. 2017). When the concentration of sodium carbonate or bicarbonate salts is varied, higher salt concentrations produce a slightly higher predicted pH, but the effect is minimal over the range of salt concentrations explored of 0.01–0.1 molal, from Postberg et al. (2009). Higher concentrations of sodium chloride salts produce a slightly lower predicted pH, due to the salinity dependence of carbonic acid dissociation constants (Millero et al. 2002) and ion–ion interactions that tend to lower activity coefficients, but the difference between a 0.05 molal NaCl ocean and a 0.2 molal NaCl ocean (the range reported in Postberg et al. 2009) is only about -0.15 pH units.

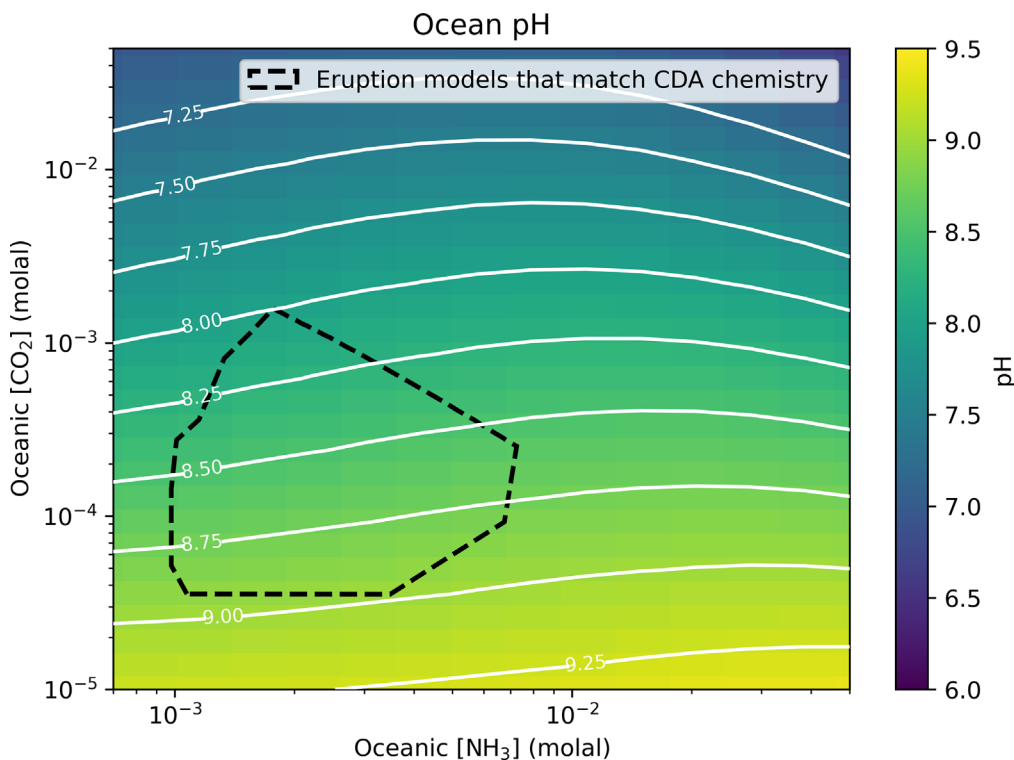


Figure 6. Our predicted pH for the ocean (plotted in color, with white contour lines of constant pH), as a function of predicted oceanic [NH₃] and [CO₂]. The dashed shape indicates the uncertainty space of our predictions for [NH₃] and [CO₂], and is the region of overlap between our physical chemistry models and allowable ion concentrations from the CDA analysis that was shown in Figure 4. Consequently, the full range of pH is that within the dashed shape. Higher concentrations of CO₂ lead to lower pH, because dissolved CO₂ acts as a weak acid, and higher concentrations of NH₃ tend to lead to higher pH, because dissolved NH₃ acts as a weak base. The pH range plotted here (8.00–9.00) is specific to the salt concentrations [NaHCO₃ or Na₂CO₃] = 0.05 molal and [NaCl] = 0.1 molal, but this pH range is very similar to our full predicted pH (~7.95–9.05) that includes the full uncertainty in ocean salt concentrations (Postberg et al. 2009).

4. Discussion

Our model results point to Enceladus’ ocean being rich in hydrogen, carbon dioxide, methane and ammonia (Figure 5). We infer dissolved gas concentrations in Enceladus’ ocean that are higher than recent estimates, which accounted for condensation of water vapor in the plumes but not fractionation during gas exsolution (Glein et al. 2015; Waite et al. 2017; Glein & Waite 2020). The gas concentrations we deduce generally sit around the 10⁻⁵–10⁻³ molal range, which in some cases are up to 4 orders of magnitude greater than the predicted concentrations of the aforementioned studies. However, we calculate lower gas concentrations than Marion et al. (2012), a study that accounted for neither condensation nor gas exsolution. Our values that fall below the no-fractionation model (Marion et al. 2012) are most easily explained by the enrichment and depletion of water vapor in the plume (relative to all other gases) during each fractionation process considered. As the plume travels upwards in the icy fissure, water vapor becomes *depleted* in the plume primarily due to condensation onto the fissure walls and secondarily due to condensation onto the solid ice grains. By contrast, during the gas exsolution process, water vapor is *enriched* in the plume due to its rapid evaporation rate. The fractionation processes compete but, as can be seen in Figure 5, condensation ultimately has a greater effect. If the opposite were true, we would find gas concentrations greater than the estimates of Marion et al. (2012).

A large portion of the uncertainty in our predicted gas concentrations arises from the wide range of fissure geometries that match observations, and the resulting wide range in

degrees of condensation that may occur during eruption (Figure 3). In particular, the outsized role that fissure depth and width at the fissure outlet play in controlling gas concentrations motivates additional modeling and observation to better constrain the shape and size of the tiger stripe fissures. The proposed Enceladus Orbilander mission includes a radar sounder in its suite of instruments (MacKenzie et al. 2021); if capable of resolving the fissure depth, width, and shape, such an instrument could prove invaluable for relating plume gas ratios to ocean gas concentrations in the future.

Although we present the results of the three distinct outgassing models separately, a combination of two or perhaps all three mechanisms are probably responsible for production of the plume gas. However, without empirical knowledge of the conditions at the ocean–plume interface, it is difficult to define the relative contributions of each process to the erupted gas. To compare overall outgassing rates from thin-film exsolution versus aerosol droplet degassing, we might consider the ratio of surface areas between the exposed portion of the ocean in the fissure, and suspended aerosol droplets just above it; if the surface areas of both are similar, then we would expect approximately equal contributions from both to the plume gas. Given that droplets freeze and degas in ~1 ms (Waite et al. 2017), we need only consider droplets up to the height at which they freeze. For droplets carried at the initial velocity of the plume gas (~3 m s⁻¹ from the condensation model), the height of droplet freezing is only on the order of centimeters. Even at much higher velocities of ~100 m s⁻¹ that reflect the speeds of grains near the plume outlet (Schmidt et al. 2008), droplets would only reach ~1 m above the ocean before freezing.

Table 2
Comparison of Enceladus' pH Range, Ocean Composition, and Differing Methodologies between this Work and Other Studies

Source	pH Range	Composition	Method Notes
Postberg et al. (2009)	8.5–9.0	NaCl—NaHCO ₃ —Na ₂ CO ₃	CDA analysis
Marion et al. (2012)	5.74–6.76	CO ₂ and CH ₄ gas hydrates	No fractionation
Hsu et al. (2015)	8.5–10.5	...	Based on silica formation
Glein et al. (2015)	10.8–13.5	Low (<10 ⁻⁷ molal) [CO ₂]	Condensation
Waite et al. (2017)	9–11, assumed	10 ⁻⁷ –10 ⁻⁴ molal [CO ₂], [CH ₄], [H ₂]	pH sets [CO ₂], other gases set relative to CO ₂
Glein & Waite (2020)	8.5–9.0	10 ⁻⁶ –10 ⁻³ molal [CO ₂]	Condensation, droplet degassing & checked against CDA analysis
This study	7.95–9.05	NaCl—NaHCO ₃ —Na ₂ CO ₃ (NH ₄)HCO ₃ —(NH ₄) ₂ CO ₃ ; 10 ⁻⁵ –10 ⁻³ molal [CO ₂], [CH ₄], [H ₂], [NH ₃]	Dynamic condensation & exsolution, comparison w/ CDA

Taking 1 m as a very conservative upper limit, a number density of $\sim 10^{12}$ micron-size droplets per m³ within 1 m of the ocean surface would be required to attain similar total surface areas between suspended aerosol droplets and the exposed ocean surface.

Could liquid aerosols be present at these number densities just above the ocean? Operating with the same assumptions of spherical, micrometer-radius, pure water-ice grains used to estimate surface areas of condensation sites in Section 2.1, we estimate a number density of ice grains near the plume outlet of $\sim 10^3$ m⁻³. Assuming that the eruption rate (in kg s⁻¹) of ice grains at the outlet is equal to the production of aerosols at the ocean, and accounting for acceleration from ~ 3 to ~ 100 m s⁻¹, we estimate droplet number densities near the ocean of $\sim 10^4$ m⁻³, or even lower in the case of tapering fissures that are wider at the ocean interface. That said, much like in the case of water vapor, it seems unlikely that the flux of ice grains is totally conserved during eruption, so further modeling or laboratory studies of the dynamics and fates of aerosols and ice grains in the plume is necessary. Supercooling of aerosol droplets could also extend the time and vertical distance over which droplets remain in the liquid phase, effectively increasing the total surface area from which gases could exsolve. An additional point of comparison may come from the vicinity of Earth's ocean surface, where aerosols are present at number densities up to 6×10^9 m⁻³ (Fitzgerald 1991). However, the conditions at Earth's ocean surface are very different from Enceladus (e.g., winds blow across Earth's oceans, while Enceladus' ocean boils), so more targeted modeling and analog studies of aerosol formation relevant to the near-vacuum pressures in the Enceladus environment are needed.

Constraining the relative contribution of the bubble formation model to outgassing on Enceladus is also difficult, requiring knowledge of the geometry of bubble nucleation sites, which could include submerged portions of the ice shell and particles (e.g., large organics) in the ocean. However, the ocean chemistries we predict (that fall within the ionic concentration restrictions of the CDA analysis) are similar between the thin-film model and boiling-dominated model. For

example, compare the dark blue and cyan error bars in Figure 5. Additionally, if one (or both) of these outgassing mechanisms produces similar fluxes to aerosol droplet degassing, then we would expect oceanic concentrations of gases and ions to fall between the lower estimates of thin-film or boiling models (blue regions in Figure 4) and the higher concentrations predicted by the droplet degassing model (the orange region in Figure 4). However, the upper limits of the thin-film and boiling-dominated models already go beyond the reasonable chemistries allowed by CDA analysis of the ice grain composition, so any contribution of droplet degassing to overall plume gas production cannot bring the predicted oceanic volatile concentrations any higher. Therefore, regardless of the dominant outgassing processes, we do not expect significant deviations from our predictions in Figure 5.

The pH we calculate for Enceladus' ocean of 7.95–9.05 is closer to neutral and more Earth-like (and possibly early Earth-like; Krissansen-Totton et al. 2018a) than recent estimates, largely due to our higher oceanic CO₂ content compared to most other estimates. As discussed in Section 1.3, estimates for Enceladus' ocean pH have varied widely, depending on how each study handled CO₂ and ultimately its concentration in the ocean (Table 2). Our pH is greater than the Marion et al. (2012) model, which has the highest concentration of oceanic CO₂ of all the models due to its assumption that the mixing ratios in the plume directly reflect the concentrations in the ocean. Our predicted pH of 7.95–9.05 has significance not only for the prospect of life on Enceladus (assuming Earth-like biochemistry, which tends to prefer circumneutral pH), but also for general comparisons of aqueous chemistry. A pH more comparable to Earth's ocean (a preindustrial value of 8.2) opens the door for more in situ Enceladus analog studies of terrestrial ocean environments, although it should be noted that Enceladus' ocean will likely have local pH variation near interfaces with other surfaces (e.g., at the ocean floor, near hypothesized hydrothermal vents).

We infer high (10⁻²–10⁻¹ molal) concentrations of ammonium ions (NH₄⁺) in the ocean, which provides support for the hypothesis that Enceladus was accreted from similar building blocks to comets. The relatively high gas

Table 3

Bulk Molecular Abundances of Volatiles for Enceladus as a Whole (this Study) Compared to Observed Ranges in Cometary Ices (Mumma & Charnley 2011)

Species	Enceladus	Cometary
NH ₃	0.001%–0.006%	0.2%–1.4%
NH ₄ ⁺	0.010%–0.163%	...
NH ₃ + NH ₄ ⁺	0.011%–0.169%	...
CH ₄	0.00001%–0.001%	0.4%–1.6%
CO ₂	0.00003%–0.001%	2%–30%
CO ₂ + CO ₃ ²⁻ + HCO ₃ ⁻	0.016–0.16%	...

concentrations that we calculate for oceanic NH₃ and the lower pH (due to high CO₂ abundance) are the cause of relatively high concentrations of NH₄⁺ in our model. Assuming that our NH₄⁺ concentration is representative of the concentration in the bulk ocean, and that NH₄⁺ is negligible in the ice shell (and core), we can estimate a *minimum* bulk abundance for the moon of 0.011%–0.169% NH₃+NH₄⁺, relative to H₂O. This bulk NH₃+NH₄⁺ abundance is close to cometary abundances of 0.2%–1.4% NH₃ relative to H₂O (Mumma & Charnley 2011; Table 3), and suggests that Enceladus' present-day NH₄⁺ may have originated as primordial NH₃ that has largely been retained through Enceladus' evolutionary history. We also note that the large (10⁻²–10⁻¹ molal) concentrations of NH₄⁺ should imply the presence of ammonium-bicarbonate ((NH₄)HCO₃) salts in the ocean, but the NH₄⁺ that was detected in ice grains has been interpreted as breakdown of organic molecules rather than salts (Khawaja et al. 2019). We note that ammonium bicarbonate and sodium carbonate have been detected on Ceres (De Sanctis et al. 2016; Vu et al. 2017; Carrozzo et al. 2018), a body that may have originated in the outer solar system (McKinnon 2012). The fact that our physical chemistry models allow NH₄⁺ concentrations >1 molal (before applying the 0.2 molal limit) may motivate quantification of a precise upper limit for NH₄⁺ in the salt-rich ice grains.

Dissolved ammonia (NH₃) is likely stable in the ocean, whereas ammonium (NH₄⁺) may be incorporated into the rock of Enceladus' core. Ammonia breakdown has previously been explored as a possible source of molecular nitrogen in the plumes (Matson et al. 2007; Sekine et al. 2015; Waite et al. 2017), but even at the high (10⁻³ molal) concentrations we predict, NH₃ decomposition into N₂ is likely minimal in Enceladus' ocean given the requirements of high temperatures (>700°C; Brandes et al. 1998), catalysts beyond the expected olivine or pyroxene outer core composition, and significant amounts of oxidants such as oxygen (Sekine et al. 2015). Furthermore, an upper limit on the volume mixing ratio of N₂ in the plume (<0.5%, Hansen et al. 2011, which translates to <0.0009 molal in our fractionation model) allows us to predict an oceanic N₂/NH₄⁺ ratio of <0.01, indicating that NH₄⁺ is by far the dominant N-bearing species in the ocean, and N₂ production is likely minimal. Dissolved NH₄⁺ can be incorporated into minerals during aqueous alteration of terrestrial basalts (Hall 1989). If similar alteration processes occur at Enceladus' ocean floor, then our estimated bulk NH₄⁺ abundance of 0.011%–0.169% relative to water may represent a lower limit for Enceladus.

Previous work noted that the CO₂ abundance in the plume and (estimated abundance) in the ocean is much lower than

typical cometary levels (e.g., McKinnon et al. 2018), and we find that this is the case for both CH₄ and CO₂ in our predictions (Table 3). When including all inorganic carbon species (CO₂, HCO₃⁻, and CO₃²⁻) that come from CO₂, we predict a bulk molecular abundance for inorganic carbon of 0.016%–0.16% relative to H₂O, which also falls short of cometary CO₂ ranges of 2%–30% (Table 3). Alteration of the core through processes such as carbonation could sequester CO₂ from the ocean. Thus cometary CO₂/H₂O is unlikely to be preserved in the aqueous phase, though the core could still contain cometary abundances in the form of carbonated rock (Glein & Waite 2020). As with NH₄⁺, the upper end of our predicted range for Enceladus' inorganic carbon (before setting the 0.2 molal limit) includes [HCO₃⁻] and [CO₃²⁻] concentrations of >1 molal (Figure 5), which is significantly higher than the estimated 0.1 molal upper limit of Na₂CO₃ or NaHCO₃ salts (Postberg et al. 2009), again suggesting the possible presence of yet-unmeasured ammonium carbonate or bicarbonate salts. The apparent issue of missing CH₄ relative to cometary levels is unresolved.

We find that Enceladus' ocean likely contains abundant energy in the H₂-CO₂ redox pair that methanogens could potentially use. In Figure 7, we compare our predictions for this available energy to Waite et al. (2017), who also found significant chemical energy available in this reaction. Because we predict a positive value for the 'apparent affinity' in the ocean, there is chemical disequilibrium in the ocean environment that life could use as a source of energy. The stoichiometric coefficients in the methanogenesis reaction (CO₂ + 4H₂ ⇌ CH₄ + 2H₂O) dictate the exponents in the reaction quotient (Equation (36)), and therefore the importance of each species' concentration on affinity, or available energy. The higher maximum available energy that we predict compared to Waite et al. (2017) thus comes primarily from the higher concentration of H₂ that we estimate for the ocean, whereas an increase in concentration of CO₂ that we predict above the estimate of Waite et al. (2017) is approximately canceled out (in calculation of the reaction quotient) by an increase in CH₄ that is the same order of magnitude.

The availability of energy for methanogenesis in Enceladus' ocean could mean that there is no life there to consume it, or that any methanogenic life is nutrient limited, and therefore unable to consume H₂ as fast as it is introduced into the ocean. In other words, there could be a small, nutrient-limited biosphere consuming only a fraction of the available energy seen in the H₂-CO₂ pair. For instance, phosphorus is vital to terrestrial life due to its incorporation in nucleotides, cell membrane lipids, and in energy-storing molecules like adenosine triphosphate, but it has not yet been detected in the plumes. Recent work suggests that the range of affinities found here and by Waite et al. (2017) could be consistent with a methanogenic community with a limited rate at which it can draw down H₂, or a limited rate of population growth due to physiological and/or environmental factors (Hoehler 2022).

5. Conclusions

We have shown that significant chemical fractionation occurs between the erupted plumes of Enceladus and the subsurface ocean from which the plumes originate. Key chemical differences arise between the easily sampled plume and the more elusive ocean as a result of the removal of water vapor from the plume via condensation on walls of the conduit

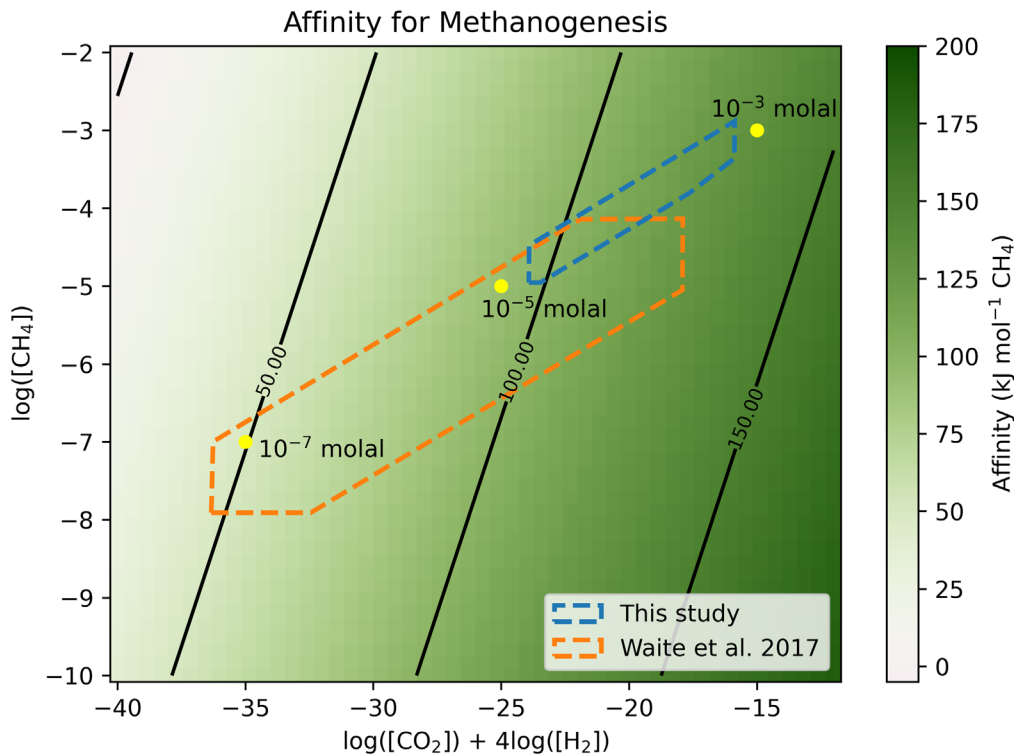


Figure 7. Apparent affinity for methanogenesis in the ocean, i.e., the available energy for methanogenesis per mole of reaction in the ocean shown as color shading and black contour lines. The x -axis represents the denominator of the reaction quotient (Equation (36)) for the methanogenesis reaction, while the y -axis represents the numerator of the reaction quotient (assuming the activity of water ≈ 1). Increasing concentrations of CO_2 or H_2 (x -axis) increase the energy per mole of reaction (i.e., methanogenesis is more favored), while increasing concentrations of CH_4 (y -axis) lower the energy per mole of reaction (i.e., methanogenesis is less favored). The region outlined by a blue dashed line encompasses the full range of our predictions for CO_2 , H_2 , and CH_4 concentrations, with upper limits applied from compatibility with CDA measurements. The region outlined by an orange dashed line encompasses the range of predictions for gas concentrations and affinity from Waite et al. (2017). The yellow circles are points of reference, indicating the affinity for hypothetical oceans with equal concentrations of CO_2 , H_2 , and CH_4 at 10^{-7} , 10^{-5} , and 10^{-3} molal. Due to higher gas concentrations overall, we predict a slightly greater maximum affinity, $\sim 130 \text{ kJ mol}^{-1} \text{ CH}_4$, for methanogenesis in Enceladus' ocean compared to Waite et al. (2017).

between the ocean and space, and by differential rates of gas exsolution from the ocean surface at the bottom of the conduit. Condensation and exsolution compete, through depletion and enrichment of water vapor in the plume, respectively, and while condensation ultimately has the greater effect, it is necessary to account for both processes to extrapolate Enceladus' ocean composition from plume measurements.

With new estimates for the gas content of the ocean, we find an ocean pH of 7.95–9.05, which encompasses the terrestrial ocean pH, high levels of NH_4^+ and inorganic carbon consistent with the accretion of Enceladus from comet-like planetesimals, and an abundance of chemical energy for potential Enceladean methanogens. We note here that our discussion of potential biology on Enceladus is decidedly biased toward terrestrial “life as we know it” (due to a lack of other examples), and therefore ocean environmental conditions such as an Earth-like pH may not necessarily be advantageous for extraterrestrial biology. Still, the availability of chemical energy from H_2 and CO_2 for methanogenesis in the ocean is independent of the chemical structure of life that uses it. Thus the statement that there is available energy for life in Enceladus' ocean need not be limited to strictly Earth-like life.

We would like to thank Christopher Glein for helpful discussions and the two anonymous reviewers for comments and suggestions that improved this paper. L.M.F. would like to thank the University of Washington Design Help Desk for their advice on figure presentation. This work was supported by the

NASA Habitable Worlds Program grant No. 80NSSC19K0311. L.M.F. is also supported by NASA FINESST award number 80NSSC21K194. All source code used in this work is freely available through Zenodo (doi:10.5281/zenodo.6633691).

Appendix A

Details of the Vapor Condensation Model

As described in Section 2.1, we adopt Nakajima and Ingersoll's (2016) model of plume formation and eruption. Conservation of mass is expressed through

$$v\delta \frac{d\rho}{dz} + \rho\delta \frac{dv}{dz} + \rho v \frac{d\delta}{dz} = E. \quad (\text{A1})$$

Here, v is velocity, δ is the fissure diameter, ρ is the plume density, z is the vertical distance (measured from the ocean surface), and E is the mass flux of vapor from the ice walls to the plume vapor (so that $E < 0$ corresponds to condensation onto the ice walls), in units of $\text{kg m}^{-2} \text{ s}^{-1}$. Conservation of momentum is expressed through

$$\rho v \delta \frac{dv}{dz} = -\delta \frac{dp}{dz} - \tau - \rho g \delta - v E^*. \quad (\text{A2})$$

Here, p is the partial pressure of the plume water vapor, τ is the stress from the ice walls ($= 12\eta v/\delta + 2C_d\rho v^2$, where η is the dynamic viscosity and C_d is the drag coefficient), g is the gravitational acceleration ($= 0.11 \text{ m s}^{-2}$), and E^* is effectively

a mass flux of sublimation from the ice walls ($E^* = E$ when $E > 0$, and $E^* = 0$ when $E < 0$).

Conservation of energy is expressed through

$$\rho v \delta \left(C_v \frac{dT}{dz} - L \frac{ds}{dz} \right) + p \delta \frac{dv}{dz} = -p v \frac{d\delta}{dz} + \frac{p}{\rho} E + v \tau + \frac{1}{2} v^2 E^* + L_H s E - \frac{\tau}{v} C_p \Delta T. \quad (\text{A3})$$

Here, C_v is the specific heat at constant volume, T is the temperature of the plume vapor, L_H is the latent heat of fusion, s is the solid mass fraction (i.e., the fractional contribution to plume mass from solid ice grains), C_p is the specific heat at constant pressure, and $\Delta T (= T - T_w)$ is the temperature difference between the vapor and the ice walls. For simplicity, we take s to be zero because we are more concerned with the dynamics of gases in the plume, and the mass fraction of ice grains does not significantly affect condensation, vapor pressures in the plume, or erupted mass fluxes (Nakajima & Ingersoll 2016).

The mass flux between the conduit walls and the plume, E , is defined by

$$E = -2 \left(\frac{p}{\sqrt{2\pi RT/M}} - \frac{p_w}{\sqrt{2\pi RT_w/M}} \right). \quad (\text{A4})$$

Here, R is the universal gas constant, M is the molar mass of water, and p_w is the temperature-dependent saturation vapor pressure over ice, defined by Equation (4).

We adopt Nakajima and Ingersoll's (2016) assumption that the latent heat flux onto the walls due to condensation is (at least partially) responsible for the elevated heat fluxes observed near the tiger stripe fissures, and that the heat flux onto the walls due to condensation (F_s) is equal to the heat flux conducted through the ice (F_c) and to the heat flux radiated from the surface (F_r). This is expressed through

$$F_s(d) = F_c(d) = F_r(d). \quad (\text{A5})$$

Here, d refers to depth ($= D - z$, where D is the full fissure depth) such that $d = 0$ at the fissure outlet. In the context of the radiated heat flux at the surface (F_r), d refers to a horizontal distance away from the fissure, again such that $d = 0$ at the fissure outlet. Heat due to condensation is found by

$$F_s(d) = -2E(d)L_H. \quad (\text{A6})$$

The conducted heat flux is approximated by

$$F_c(d) = 4k \frac{T_s(d) - T_w(d)}{\pi d}. \quad (\text{A7})$$

Here, k is the thermal conductivity of ice, and $T_s(d)$ is the surface temperature at horizontal distance d away from the fissure. The radiated heat flux is found by

$$F_r(d) = 2\sigma(T_s^4(d) - T_e^4). \quad (\text{A8})$$

Here, σ is the Stefan–Boltzmann constant, and T_e is the effective temperature of the ice (≈ 68 K).

To initialize the model, we begin by guessing a value for the pressure at the base of the fissure, p_0 , just above the ocean surface. Assuming a vapor temperature at the base of the fissure, T_0 , that is equal to the temperature of the liquid (≈ 273 K) enables us to find the density of the vapor ρ_0 via the

ideal gas law. Using Equation (5), which describes the evaporation rate from water, we are able to find the plume velocity at the base of the fissure, v_0 . In general, we then use Equations (A1), (A2), and (A3), along with Equation (2), the ideal gas law, and an equation for the internal energy ($du = C_v dT$) to solve for each term dT/dz , du/dz , ds/dz , $d\rho/dz$, dp/dz , and dv/dz (six equations and six unknowns). Note that E and T_w are two additional unknowns that appear in the mass, energy, and momentum conservation equations, and we take two different approaches to solve for these, described in the next paragraphs. We then use a finite-difference method to approximate each variable (T , u , s , ρ , p , and v) slightly further up in the fissure conduit (e.g., $T(z_0 + \Delta z) = T_0 + (dT/dz)_0 \times \Delta z$), and repeat until we reach the top of the fissure, where $z = D$. We use the bisection method to iteratively adjust our initial guess for p_0 until we reach a solution where the velocity at the fissure outlet is equal to one of our velocity boundary conditions (either the sound speed or the escape velocity).

As in Nakajima & Ingersoll (2016), we take two approaches to modeling the condensation and heat fluxes, and find minimal differences in the results between the two approaches. The first approach is less computationally intensive, and involves a semianalytic solution to Equations (A5), (A6), (A7), and (A8). In this semianalytic approach, we begin by assuming that the temperature of the wall, T_w , is constant and equal to 273 K at all vertical distances z . We then use a numerical solver to solve Equations (A5), (A6), (A7), and (A8), in particular to find the mass flux between fissure walls and the plume $E(d)$ (or, equivalently, $E(z)$ which is the same array of values in reverse order).

In the second approach, we make no assumptions about the temperature of the wall, and instead find a fully numerical solution to the condensation and heat flux Equations (A4)–(A8). The fully numerical approach necessitates solving the Equations (A4)–(A8) at each finite distance z_n , by first finding $T(z_n)$ and then solving (A4)–(A8) for the wall temperature at that depth, $T_w(d_n = D - z_n)$, surface temperature at an equivalent horizontal distance away from the fissure, $T_s(d_n = D - z_n)$, and mass flux between the plume and fissure walls at that depth, $E(d_n = D - z_n)$. With these values calculated, we can proceed to find dT/dz , du/dz , ds/dz , $d\rho/dz$, dp/dz , and dv/dz , as before, and again use the finite-difference method to find T , u , s , ρ , p , and v all the way up the fissure.

Appendix B

Activity Coefficients from Pitzer Parameters

To calculate activity coefficients for dissolved ionic species we use the Pitzer equations, which are appropriate for ionic strengths $I > 0.5$ molal (Marion & Kargel 2008). Ionic strength can be calculated via

$$I = \frac{1}{2} \sum_i m_i z_i^2. \quad (\text{B1})$$

Here, m_i and z_i are the molality and charge of ionic species i .

The activity coefficients are determined from Pitzer parameters that are specific to binary and ternary interactions between aqueous ionic and neutral species. For simplicity, we ignore the effects of ternary interactions and any neutral–ion and neutral–neutral interactions, assuming activity coefficients of the neutral species $\text{NH}_3(\text{aq})$ and $\text{CO}_2(\text{aq})$ as equal to 1. Ternary interactions can be discounted at ionic strengths < 3.5 molal (Langmuir 1997), and we generally predict ionic

strengths around 1 molal. Neutral–ion interactions are only relevant at particularly high concentrations of neutral species (Marion & Kargel 2008). Marion et al. (2012) have also previously estimated the activity coefficient for ammonia at low temperatures (~ 273 K) to be ≈ 1 . We also ignore cation–cation and anion–anion interactions because the parameters describing these interactions are not widely reported, and in particular are unavailable for NH_4^+ (Marion et al. 2012).

The following equations and notation for the calculation of Pitzer parameters are adopted from Krissansen-Totton et al. (2018b), who used the same simplifications as the Pitzer model described in the previous paragraph, and from Marion & Kargel (2008), where the full versions of all equations can be found.

Activity coefficients for cations (M) and anions (X) are found via

$$\ln(\gamma_M) = z_M^2 F + \sum_{\text{all anions}} m_a (2B_{Ma} + ZC_{Ma}), \quad (\text{B2})$$

$$\ln(\gamma_X) = z_X^2 F + \sum_{\text{all cations}} m_c (2B_{cX} + ZC_{cX}). \quad (\text{B3})$$

Here,

$$F = -A_\phi \left[\frac{I^{0.5}}{1 + bI^{0.5}} + \frac{2}{b} \ln(1 + bI^{0.5}) \right] + \sum_{\text{all pairs}} m_a m_c B'_{ca}, \quad (\text{B4})$$

$$Z = \sum_i m_i |z_i|, \quad (\text{B5})$$

$$B_{\text{MX}} = B_{\text{MX}}^{(0)} + B_{\text{MX}}^{(1)} f(\alpha_1 I^{1/2}) + B_{\text{MX}}^{(2)} f(\alpha_2 I^{1/2}), \quad (\text{B6})$$

$$f(x) = \frac{2[1 - (1+x)\exp(-x)]}{x^2}, \quad (\text{B7})$$

$$B'_{\text{MX}} = \frac{B_{\text{MX}}^{(1)} f'(\alpha_1 I^{1/2})}{I} + \frac{B_{\text{MX}}^{(2)} f'(\alpha_2 I^{1/2})}{I}, \quad (\text{B8})$$

$$f'(x) = \frac{-2[1 - (1+x+x^2/2)\exp(-x)]}{x^2}, \quad (\text{B9})$$

$$C_{\text{MX}} = \frac{C_{\text{MX}}^\phi}{2 |z_M z_X|^{1/2}}. \quad (\text{B10})$$

In the above equations, the subscripts c and a refer to cations and anions, respectively. As in Equation (B1), m refers to molality and z refers to charge. In Equations (B2) and (B3), the B and C terms are Pitzer parameters that account for specific cation–anion interactions, and they are derived from Equations (B6) and (B10), respectively. In Equation (B4), $A_\phi = 0.3915 \text{ kg}^{0.5} \text{ mol}^{-0.5}$ and $b = 1.2 \text{ kg}^{0.5} \text{ mol}^{-0.5}$ are constants. In Equations (B6) and (B8), α_1 and α_2 are constants. In the case of all binary systems except 2:2 electrolytes, $\alpha_1 = 1.4 \text{ kg}^{0.5} \text{ mol}^{-0.5}$ and $\alpha_2 = 0 \text{ kg}^{0.5} \text{ mol}^{-0.5}$. Because all ion–ion pairs considered here fall under this category (most are 1:1, except for pairs involving CO_3^{2-} , which are 1:2), $\alpha_2 = 0 \text{ kg}^{0.5} \text{ mol}^{-0.5}$, which allows us to ignore the third term in Equation (B6) and the second term in (B8). The Pitzer parameters $B^{(0)}$, $B^{(1)}$, and C^ϕ are reported in Marion & Kargel (2008) and Marion et al. (2012), and set to 0 where unavailable.

The activity of water, a_w , is calculated from

$$a_w = \exp\left(\frac{-\phi \sum_i m_i}{55.50844}\right). \quad (\text{B11})$$

Here, ϕ is the osmotic coefficient, given from

$$(\phi - 1) = \frac{2}{\sum_i m_i} \left[\frac{-A_\phi I^{3/2}}{1 + bI^{1/2}} + \sum_{\text{all pairs}} m_c m_a (B_{ca}^\phi + ZC_{ca}) \right]. \quad (\text{B12})$$

Appendix C Solvation Energies of Ions

While dissolved ions such as Na^+ , Cl^- and NH_4^+ are included in our aqueous chemistry model (Section 2.4), we do not include them in our exsolution models (Section 2.3) due to their high energies of solvation. For example, NH_4^+ has a solvation energy (W_{sol} , the energy difference between the gas phase and dissolved phase) of $-88.2 \text{ kcal mol}^{-1}$ ($-3.69 \times 10^{-5} \text{ J mol}^{-1}$, $-6.13 \times 10^{-19} \text{ J molecule}^{-1}$; Meot-Ner 1987). We can find a ratio of the number densities of NH_4^+ in the vapor phase versus the dissolved phase (Postberg et al. 2009, Supplementary Material) via

$$\frac{n_v}{n_l} \simeq n_l \exp\left(\frac{W_{\text{sol}}}{k_B T}\right). \quad (\text{C1})$$

Here, n_v is the number density of a solute (e.g., NH_4^+) in the vapor phase, n_l is the number density of the solute in the liquid, W_{sol} is the solvation energy (here in units of J molecule^{-1}), k_B is the Boltzmann constant (here in units of J K^{-1}), and T is the temperature (taken to be 273.15 K). For NH_4^+ , we find this ratio to be on the order of 10^{-70} . For context, the same ratio n_v/n_l for NH_3 is much greater, $\sim 2 \times 10^{-3}$ at 273 K. The equation to calculate this ratio for NH_3 or other gases with known Henry's law constants is

$$\frac{n_v}{n_l} = \frac{1}{\alpha} = \frac{M_{\text{H}_2\text{O}}}{HRT\rho_l}. \quad (\text{C2})$$

Here, α is the Bunsen coefficient (a dimensionless version of the Henry's law constant; Sander 2015), $M_{\text{H}_2\text{O}}$ is the molar mass of water, H is the Henry's law constant in units of Pa^{-1} , R is the gas constant, T is the temperature, and ρ_l is the density of water.

ORCID iDs

Lucas M. Fifer  <https://orcid.org/0000-0003-0373-9110>
David C. Catling  <https://orcid.org/0000-0001-5646-120X>
Jonathan D. Toner  <https://orcid.org/0000-0003-1681-6189>

References

- Affholder, A., Guyot, F., Sauterey, B., Ferrière, R., & Mazevet, S. 2021, *NatAs*, 5, 805
- Bandura, A. V., & Lvov, S. N. 2006, *JPCRD*, 35, 15
- Baptiste, É, Brochier, C., & Boucher, Y. 2005, *Archaea*, 1, 859728
- Bates, R. G., & Pinching, G. D. 1949, *J. Res. Natl. Bur. Stand.*, 42, 419
- Bouquet, A., Glein, C. R., & Waite, J. H. 2019, *ApJ*, 873, 28
- Bradley, A. S. 2016, *PNAS*, 113, 13944
- Brandes, J. A., Boctor, N. Z., Cody, G. D., et al. 1998, *Natur*, 395, 365
- Broecker, W. S., & Peng, T.-H. 1982, *Tracers in the Sea* (Palisades, NY: Lamont-Doherty Geological Observatory of Columbia Univ.), https://www.ldeo.columbia.edu/~broecker/Home_files/TracersInTheSea_searchable.pdf
- Cable, M. L., Porco, C., Glein, C. R., et al. 2021, *PSJ*, 2, 132
- Carrozzo, F. G., De Sanctis, M. C., Raponi, A., et al. 2018, *SciA*, 4, 1
- Choblet, G., Tobie, G., Sotin, C., et al. 2017, *NatAs*, 1, 841

- Cussler, E. L. 2009, *Diffusion: Mass Transfer in Fluid Systems* (3rd ed.; Cambridge: Cambridge Univ. Press)
- De Sanctis, M. C., Raponi, A., Ammannito, E., et al. 2016, *Natur*, **536**, 54
- Fierer, N., & Jackson, R. B. 2006, *PNAS*, **103**, 626
- Fitzgerald, J. W. 1991, *AtmEB*, **25**, 533
- Frössling, N. 1938, *Gerlands Beiträge Geophys*, **52**, 170
- Glein, C. R., Baross, J. A., & Waite, J. H. 2015, *GeoCoA*, **162**, 202
- Glein, C. R., & Waite, J. H. 2020, *GeoRL*, **47**, e85885
- Goguen, J. D., Buratti, B. J., Brown, R. H., et al. 2013, *Icar*, **226**, 1128
- Hall, A. 1989, *GeocJ*, **23**, 19
- Hansen, C. J., Shemansky, D. E., Esposito, L. W., et al. 2011, *GeoRL*, **38**, L11202
- Hansen, C. J., Esposito, L. W., Aye, K.-M., et al. 2017, *GeoRL*, **44**, 672
- Hansen, C. J., Esposito, L. W., Colwell, J. E., et al. 2020, *Icar*, **344**, 113461
- Hedman, M. M., Dyingra, D., Nicholson, P. D., et al. 2018, *Icar*, **305**, 123
- Hemingway, D. J., Rudolph, M. L., & Manga, M. 2019, *NatAs*, **4**, 234
- Higbie, R. 1935, *Transactions of the AIChE*, **31**, 365
- Higgins, P. M., Glein, C. R., & Cockell, C. S. 2021, *JGRE*, **126**, e06951
- Hoch, M. P., Fogel, M. L., & Kirchman, D. L. 1992, *LimOc*, **37**, 1447
- Hoehler, T. M. 2022, *NatAs*, **6**, 4
- Hsu, H. W., Postberg, F., Sekine, Y., et al. 2015, *Natur*, **519**, 207
- Ingersoll, A. P., & Pankine, A. A. 2010, *Icar*, **206**, 594
- Ingersoll, A. P., & Nakajima, M. 2016, *Icar*, **272**, 319
- Jayaweera, G. R., & Mikkelsen, D. S. 1990, *SSASJ*, **54**, 1447
- Jayaweera, G. R., Paw, K. T. U., & Mikkelsen, D. S. 1990, *SSASJ*, **54**, 1462
- Jones, S. F., Evans, G. M., & Galvin, K. P. 1999, *AdCIS*, **80**, 27
- Keller, M., & Zengler, K. 2004, *Nature Reviews Microbiology*, **2**, 141
- Kempf, S., Srama, R., Postberg, F., et al. 2005, *Sci*, **307**, 1274
- Kempf, S., Beckmann, U., & Schmidt, J. 2010, *Icar*, **206**, 446
- Khawaja, N., Postberg, F., Hillier, J., et al. 2019, *MNRAS*, **489**, 5231
- Kieffer, S. W., Lu, X., Bethke, C. M., et al. 2006, *Sci*, **314**, 1764
- Kite, E. S., & Rubin, A. M. 2016, *PNAS*, **113**, 3972
- Kocamustafaogullari, G. 1983, *ICHMT*, **10**, 501
- Krissansen-Totton, J., Arney, G. N., & Catling, D. C. 2018a, *PNAS*, **115**, 4105
- Krissansen-Totton, J., Olson, S., & Catling, D. C. 2018b, *SciA*, **4**, eaao5747
- Landau, L. D., & Lifshitz, E. M. 1959, *Fluid Mechanics* (London: Pergamon), 364
- Langmuir, D. 1997, *Aqueous Environmental Geochemistry* (Upper Saddle River, New Jersey: Prentice Hall)
- Liger-Belair, G. 2012, *EPJST*, **201**, 1
- MacKenzie, S. M., Neveu, M., Davila, A. F., et al. 2021, *PSJ*, **2**, 77
- Magee, B. A., & Waite, J. H. 2017, *LPSC*, **48**, 2974
- Marion, G. M., & Kargel, J. S. 2008, *Cold Aqueous Planetary Geochemistry with FREZCHEM. Advances in Astrobiology and Biogeophysics* (Berlin: Springer)
- Marion, G. M., Kargel, J. S., Catling, D. C., & Lunine, J. I. 2012, *Icar*, **220**, 932
- Matson, D. L., Castillo, J. C., Lunine, J., & Johnson, T. V. 2007, *Icar*, **187**, 569
- McCollom, T. M. 2016, *PNAS*, **113**, 13965
- McCollom, T. M., & Seewald, J. S. 2006, *E&PSL*, **243**, 74
- McKay, C. P., Porco, C. C., Altheide, T., Davis, W. L., & Kral, T. A. 2008, *AsBio*, **8**, 909
- McKinnon, W. B. 2012, *LPI Contribution*, **1667**, 6475
- McKinnon, W. B., Lunine, J. I., Mousis, O., Waite, J. H., & Zolotov, M. Y. 2018, in *Enceladus and the Icy Moons of Saturn*, ed. P. M. Schenk et al. (Tucson, AZ: Univ. Arizona Press), 17
- Meot-Ner, M. 1987, *JPhCh*, **91**, 417
- Millero, F. J., Pierrot, D., Lee, K., et al. 2002, *DSRI*, **49**, 1705
- Montes, F., Rotz, C. A., & Chaoui, H. 2009, *Transactions of the ASABE*, **52**, 1707
- Mumma, M. J., & Charnley, S. B. 2011, *ARA&A*, **49**, 471
- Murphy, D. M., & Koop, T. 2005, *QJRM*, **131**, 1539
- Nakajima, M., & Ingersoll, A. P. 2016, *Icar*, **272**, 309
- Nimmo, F., Spencer, J. R., Pappalardo, R. T., & Mullen, M. E. 2007, *Natur*, **447**, 289
- Nock, W. J., Heaven, S., & Banks, C. J. 2016, *ChEnS*, **140**, 171
- Park, S. H., Park, C., Lee, J. Y., & Lee, B. 2017, *Nucl. Eng. Technol.*, **49**, 692
- Perrin, C. L., & Engler, R. E. 1991, *JPhCh*, **95**, 8431
- Persad, A. H., & Ward, C. A. 2016, *ChRv*, **116**, 7727
- Porco, C. C., Helfenstein, P., Thomas, P. C., et al. 2006, *Sci*, **311**, 1393
- Postberg, F., Kempf, S., Schmidt, J., et al. 2009, *Natur*, **459**, 1098
- Postberg, F., Khawaja, N., Abel, B., et al. 2018, *Natur*, **558**, 564
- Postberg, F., Schmidt, J., Hillier, J., Kempf, S., & Srama, R. 2011, *Natur*, **474**, 620
- Rayleigh, L. 1917, *The London, Edinburgh, and Dublin Philosophical Magazine and Journal of Science*, **34**, 94
- Reeves, E. P., & Fiebig, J. 2020, *Elements*, **16**, 25
- Reh, K., Spilker, L., Lunine, J. I., et al. 2016, in *2016 IEEE Aerospace Conf. (Piscataway, NJ: IEEE)*, 1
- Sander, R. 2015, *ACP*, **15**, 4399
- Schmidt, J., Brilliantov, N., Spahn, F., & Kempf, S. 2008, *Natur*, **451**, 685
- Sekine, Y., Shibuya, T., Postberg, F., et al. 2015, *NatCo*, **6**, 8604
- Spencer, J. R., Nimmo, F., Ingersoll, A. P., et al. 2018, in *Enceladus and the Icy Moons of Saturn*, ed. P. M. Schenk et al. (Tucson, AZ: Univ. Arizona Press), 163
- Taubner, R. S., Pappenreiter, P., Zwicker, J., et al. 2018, *NatCo*, **9**, 748
- Teolis, B. D., Perry, M. E., Hansen, C. J., et al. 2017, *AsBio*, **17**, 926
- Thomas, P. C., Tajeddine, R., Tiscareno, M. S., et al. 2016, *Icar*, **264**, 37
- Vu, T. H., Hodyss, R., Johnson, P. V., & Choukroun, M. 2017, *P&SS*, **141**, 73
- Waite, J. H., Combi, M. R., Ip, W.-H., et al. 2006, *Sci*, **1419**, 1419
- Waite, J. H., Glein, C. R., Perryman, R. S., et al. 2017, *Sci*, **356**, 155
- Waite, J. H., Lewis, W. S., Magee, B. A., et al. 2009, *Natur*, **460**, 487